# Synthesis of Multiphase Binary Eutectic Al-Mg Alloy-Nanoparticles by Electrical Wire Explosion Technique for High-Energy Applications, its Characterisation and Size-Dependent Thermodynamic and Kinetic Study

**L Santhosh Kumar[a], S R Chakravarthy[a], Raviraj Verma[b], R Jayaganthan[c,*], R Sarathi[d] and A Srinivasan[e]**

[a] Centre of Propulsion Technology, National Centre for Combustion Research and Development, Dept. of Aerospace Engineering, IIT Madras, Chennai-36, India
[b] Dept. of Metallurgical and Materials Engineering, IIT Roorkee, Roorkee-67, India
[c] Dept. of Engineering Design, IIT Madras, Chennai-36, India
[d] Dept. of Electrical Engineering, IIT Madras, Chennai-36, India
[e] Division of Materials Science and Technology, NIIST, Trivandrum-19, India
[*] Author of correspondence
**E-mail: edjay@iitm.ac.in**

## Abstract:

In the present study, Al-Mg binary eutectic alloy nanoparticles were synthesized through the electrical wire explosion technique (EWET) in an inert ambience. High-speed imaging was carried out to visualize sublimation process of alloy wire and subsequent formation of nanoparticle through the condensation process. The fundamental gas-phase kinetics is investigated by the embedded atom method (EAM) and reactive hard-sphere model to elucidate the mechanisms governing the formation of finer particles of eutectic AlMg alloy. The condensed phase transformations are analysed through size-dependent thermodynamics and growth kinetics modelling, which has shown that the adsorption controlled growth is responsible for the generation of polydispersed particles. The formation of $Al_{20}Mg_{23}$ nanoparticles and its morphological features were characterised through XRD and SEM/EDS analysis. High-resolution transmission electron microscopy (HRTEM) along with the selected area electron diffraction (SAED) confirmed the spherical morphology, crystallinity, lognormal particle size distribution and the multiphase microstructure of the eutectic AlMg nanoparticles. The formation of multiphase alloy nanoparticles is attributed to the insignificant difference in melting temperatures of Al and Mg and phase boundary modifications due to size-effect. Scanning transmission electron microscopy (STEM) revealed the spatial distribution of Al and Mg within the alloy nanoparticle. Differential scanning calorimetry (DSC) confirmed the reduction in melting temperature and fusion enthalpy of eutectic Al-Mg alloy nanoparticles. It is proposed as a potential substitute for Al nanoparticles to reduce the ignition temperature, agglomeration and two-phase flow losses for realising improved combustion performance in solid rocket propellants.

## Keywords:

Eutectic alloy nanoparticles, Multiphase microstructure; Collision flux; Non-equilibrium quenching; Adsorption controlled growth; Solid rocket propellants; Ignition temperature; Combustion performance; Electrical wire explosion

## 1. Introduction:

In recent years, applications of metal-alloy nanoparticles have gained substantial scientific and technological significance which consequently led to the development of varied synthesis routes and advancements. A myriad of nanopowders has been synthesized by various techniques involving gas-phase chemical reactions. These aerosol processes are proved to be advantageous over other conventional wet-chemistry synthesis routes. The wet chemical methods involve a bottom-up approach in which molecular precursors react to form various types of nanostructures. Some of the wet-chemistry techniques used for the synthesis of nanoparticles are the sol-gel method, chemical precipitation, micro-emulsion method, hydrothermal method, electrochemical reduction and thermal and photochemical decomposition. Although these wet chemical routes can synthesize unagglomerated and relatively monodispersed nanoparticles, their yield is less and reproducibility is generally less as the composition is very sensitive to the reaction conditions [1]. Additional limitations of monomer concentration gradients and temperature could affect the scalability of the wet processes. Despite the advantage of better control over particle dimensions in these techniques, the templates and surface-bound residues would significantly affect the surface chemistry of the nanoparticles, if not removed properly [2]. In the gas-phase synthesis routes, the metal vapours react to produce product-clusters that nucleate and grow further by molecular collisions, particle coalescence and coagulation [3]. The process-control parameters of the synthesis route greatly influence the nanoparticle purity, size-distribution and the yield. The dominance of the gas-phase synthesis processes can be ascribed to the following reasons: (i) rapid reactant mixing on a molecular scale (ii) high purity nanoparticle synthesis capabilities (iii) ease of separation of nanopowders from the gaseous medium (iv) easily tuneable process parameters for tailoring the properties and (v) energy efficient. Alloy nanoparticles are found to be quintessential in catalytic, magnetic, mechanical, optical, electronic and energetic applications because of their tunable compositions [4-6]. Metal-alloy nanopowders are advantageous as fuel additives in enhancing the performance of energetic formulations of solid-propellants, pyrotechnics and explosives [7-9]. Recent research is focused on reactivity enhanced Al-based alloy powders rather than pure aluminium powders in high energy applications [10]. Al-Mg alloy powders exhibit high combustion enthalpies with reduced ignition delays and high energy densities [11-15].

The energetic materials applications have relied upon Al-Mg alloys for a long time. One of their first applications was in the formulation of pyrotechnics [16-18] while more recently; they have been successfully used as additives in propellants [19] and the chemical gas generators [20]. As a result of alloying, the alloy nanoparticles exhibit very complex crystal structures and unique chemical and physical characteristics [21-24] that are not typical of their component metals. The bifunctional enhancement in the catalytic and the thermochemical properties have made them find varied applications in the field of rocket propellants and catalysis. By the virtue of high surface free energy and surface to volume ratio, the alloy nanoparticles possess a strong tendency to melt and coalesce at the temperatures much lower than their melting point. In addition to this, the binary eutectic composition i.e., the composition of the binary alloy system which is characterized by the

lowest melting temperature of the system will further decrease the melting temperature. It has been reported that the Al-Mg alloys exhibit very low ignition temperatures in comparison to pure Al [25]. The closely collaborated interplay of compositional effect and the size-effect is expected to reduce the melting temperature further, which consequently brings down the ignition temperature, ignition delay and agglomeration in the propellants.

Ultrafine metal particles and their compounds have been synthesized by high-energy electrical explosion of wires [26-27]. The electrical wire explosion causes a very high rate of changes in the thermodynamic parameters of the system which are attained by the flow of electric current through the metal wire with a current density of $10^6$-$10^9$ A/cm$^2$ [28]. This results in the explosive transition of metal wire to a state of plasma. Thus formed plasma expands at the rates of several miles per second, subsequently allowing the mixture to cool at the rate up to $10^{10}$ K/s [29]. It has been reported that various metal-based solid-solutions and intermetallic alloy nanopowders can be synthesized by using the wire explosion technique (WET) [30-32]. Also, an eclectic variety of metal, metal-oxide, metal-carbide and metal-nitride nanopowders have been synthesized economically by the WET [33-40]. The literature on the size-dependent thermodynamic and diffusional analysis of bimetallic eutectic-alloy nanoparticle formation mechanism in the WET is scarce. Therefore, the present work is focused on synthesizing Al-Mg nanoparticles by exploding the eutectic Al-Mg alloy wire in an inert ambience of argon and helium gas and subsequently characterizing the ultrafine particles to confirm the formation of nanosize eutectic alloy nanoparticles through experiments. The alloy nanoparticle formation mechanism and its dependence of size-effect are explained through size-dependent thermodynamic, kinetic and diffusion modelling.

In the present work, an endeavour has been made to synthesize Al-Mg binary eutectic nanoparticles by wire explosion technique and the following significant aspects are deliberated: (i) Light microscopy to observe the microstructure of the homogenized Al-Mg eutectic wire. (ii) Energy dispersive analysis of X-rays (EDAX) through scanning electron microscopy (SEM) to identify the phase compositions of the wire material. (iii) X-ray diffraction study to understand the existence of various phases and their transition upon the eutectic nanoparticle formation. (iv) Analysis of particle morphology and size-distribution through high-resolution transmission electron microscopy (HRTEM). (v) Line-EDAX to analyse the compositional variation of Al and Mg across the nanoparticles, aided by HRTEM. (vi) Selected area electron diffraction (SAED) analysis to envisage the configuration of phases in the nanoparticles and their crystallinity. (vii) Differential scanning calorimetry (DSC) to understand the thermal behaviour, melting temperature and the enthalpy of fusion of the synthesized alloy nanoparticles. (viii) Size-dependent thermodynamic and diffusional modelling studies to understand the nucleation energetics and effect of diffusion on alloy-nanoparticle growth and (ix) Corresponding effect of Al-Mg eutectic alloy nanoparticles on the ignition temperature and agglomeration in the propellants.

## 2. Experimental Studies

The eutectic Al-Mg alloy nanoparticles were synthesized by electrically exploding the Al-Mg eutectic alloy wire in an explosion chamber with an inert ambience. The eutectic alloy block was cast mixing 34.45 wt% of Mg and 65.55 wt% of Al in a marginally eutectic proportion, with argon purging. The wires of diameter 1 mm required for the wire explosion process were cut from the cast alloy blocks using electrical discharge machining (EDM). The alloy wires were cleaned with acetone to remove any surface contaminants, before usage in the explosion process. The basic electrical circuit of the wire explosion setup is shown in **Fig. 1a**. which is used to synthesize the eutectic Al-Mg alloy nanoparticles upon the explosion of the alloy wire as shown in **Fig. 1b**. The electrical WET is a physical vapour deposition route in which a thin conducting wire is sublimated by discharging a bank of high voltage capacitors through it. The vapour so formed is allowed to expand adiabatically and eventually cools down as a consequence of collisions with the ambient gas molecules forming a supersaturated vapour which solidifies as nanoparticles by homogeneous nucleation [41].

The experimental setup comprises of a cylindrical sapphire explosion chamber connected with a vacuuming system to maintain the inertness of the system, and electrical terminals to allow for the capacitors to discharge through the conducting alloy wire. The capacitor bank is charged to the required voltage using a voltage-doubler circuit so that the stored energy ($W$) is $½CV^2$, where $C$ is the capacitance and $V$ is the charging voltage. The circuit used in the present work functions as an underdamped RLC circuit, satisfying the condition

$$\frac{R^2}{4L^2} < \frac{1}{LC} \tag{1}$$

and thereby delivering the energy of $W=V\times I\times t$ in a time period $t$. The nanoparticle size can be controlled by varying the energy deposited on the wire by appropriately changing the electrical parameters and controlling the explosion chamber pressure. The electrical parameters used for synthesizing the alloy nanoparticles are provided in **Table 1**.

**Table 1**. Circuit parameters used in the eutectic alloy-wire explosion.

| Parameter | Values |
|---|---|
| Material | Al-Mg alloy |
| Length of the wire | 60 mm |
| Diameter of the wire | 1 mm |
| Charging voltage | 30 kV |
| Capacitance | 3 **µ**F |
| Chamber pressure | 25 kPa |

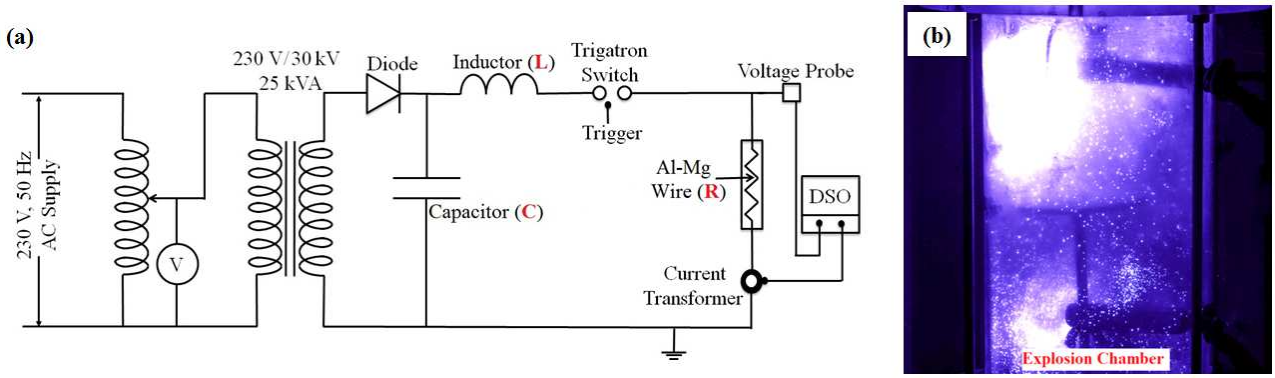


**Fig. 1.** (a) Circuit diagram of the wire explosion setup and (b) the wire explosion process.

A current probe (Pearson Electronics, Model No-101) and a voltage probe (PEEC. A, EP-50k) were used to measure the current flow through the alloy wire (R) and the voltage across its ends respectively, during the explosion. The characteristic current and voltage waveform of the wire explosion process is shown in **Fig. 2**. In the present work, X-ray diffraction study was done by using Bruker D8 diffractometer with Cu-Kα radiation of wavelength 1.5425 Å, at the scan rate of $10^0$ per minute. Transmission electron microscopy was used to determine the particle morphology and the size-distribution using Oxford Instruments and Jeol JEM 3200FS TEMs. Scanning electron microscopy was performed using FEI Quanta FEG 200 with an additional attachment of energy dispersive analysis of X-rays (EDAX) to investigate the elemental composition of the alloy nanoparticles. Differential scanning calorimetry was carried out to understand the thermal characteristics of the alloy nanoparticles using Netzsch STA 449F3 calorimeter with a heating rate of 10 K/min in an ambience of ultra-high pure argon gas.

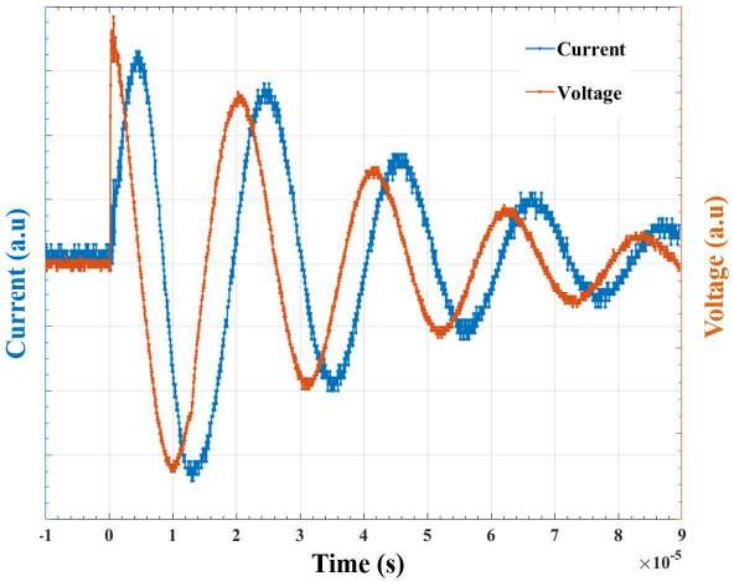


**Fig. 2**. Current and voltage waveforms during the alloy-wire explosion.

## 3. Mechanisms of Alloy-nanoparticle Formation

The design of alloy nanoparticles with tunable shapes, sizes, structures and compositions is a significant pathway towards active, robust and efficient utilization of their size-dependent properties in diverse applications. Alloy nanoparticles differ from their bulk counterparts in various significant aspects in terms of mixing, microstructure and their geometric shapes [42]. Currently, there is no generic formation mechanism available to explain the binary alloy nanoparticle formation through wire explosion process. Hence, it is very essential to understand the gas-phase formation mechanism of alloy nanoparticles, critical parameters of the wire explosion process that govern their properties and the thermodynamics and kinetics involved in the evolution of their microstructure. In the present work, we propose an alloy nanoparticle formation formalism that considers the molecular regime kinetics involved in the gas phase reactions, size-dependent alloying and diffusion assisted growth that eventually lead to the formation of lognormally distributed alloy nanoparticles with compositional variations. This formalism explains the effect of the mean free path and collision flux on the size distribution of the alloy nanoparticle and predicts their formation zones inside the explosion chamber. Also, the configurationally driven reasons for the deviation of alloy nanoparticle composition from the stoichiometry are elucidated and the steps involved in the formation of Al-Mg eutectic alloy nanoparticle formation, the microstructure evolution and the limitations on the substitutional alloying ability are discussed in detail.

In this alloy nanoparticle formation formalism, the preliminary chemical reactions are assumed to take place in the gaseous phase forming the gas-phase products, which eventually condense as alloy nanoparticles with non-equilibrium microstructures. When the capacitor bank ($C$) charged to the required voltage ($V$) is discharged through the alloy-wire, the energy ($W$) deposited on the wire sublimates it and a binary reactive gaseous mixture is produced in the inert argon ambience. The electrical energy ($W$) deposited on the wire and the sublimation energy ($W_s$) required to sublimate the wire is given by the expressions

$$W = \frac{1}{2} C V^2 \tag{2}$$

$$W_s = C_s.\Delta T_m + h_m + C_l.\Delta T + h_g \tag{3}$$

where $C_s$ is the heat capacity of the solid alloy wire, $C_l$ is the heat capacity of the molten alloy, $h_m$ and $h_g$ are the latent heat of melting and heat of evaporation of the alloy, respectively, $\Delta T_m = T_m - T_0$ and $\Delta T = T - T_m$. When the Al-Mg eutectic alloy wire is sublimated, it forms a cloud of partially or completely ionized plasma depending on the magnitude of the energy deposited on the wire. We have shown in our previous work that, various sequential phase transformations, dissociations, ionization and recombination mechanisms could be understood by Born-Haber cycle [43]. In this reactive cloud, only the Al and Mg atoms are reactively contributing to spontaneous alloying whereas the background argon gas remains inert and unreactive at all operating temperatures and pressures. Argon gas, being inert, only

offers collision surfaces in altering the kinetic energy of the reactive Al and Mg atoms thereby contributing to the reduction in the mean temperature of the reactive mixture.

The dynamics of the reacting species is explained with the help of the kinetic theory of reactive gases treating the atoms as reactive hard-spheres with their kinetic energy alone contributing to the activation energy ($\Delta G^{*}$) required for the productive reactions. These gas-phase products are the result of the successful reactive gaseous collisions which eventually form the final condensed phase microstructures in the alloy-nanoparticles. Embedded atom method (EAM) is adopted here to explain the atomistic pairing-up of the Al and Mg atoms and formation of their eutectic alloy clusters. The reactive species that have failed to cross the free energy barrier and collide with a threshold kinetic energy fail to pair-up reactively and remain in their gaseous reactant state. Excess energy deposition on the alloy wire during the explosion makes the individual reactants cross the free energy threshold and collide reactively. Supersaturation upon explosion and the non-equilibrium quenching of the gaseous products pertaining to a huge temperature difference between them and the ambient gas leads to the formation of ultrafine particles directly from the gas phase. If the gaseous products undergo equilibrium cooling due to insufficient energy absorption and localized temperature and pressure perturbations, then the gas-liquid-solid transformation results, leading to the formation of coarse particles. The alloy nano-droplets formed during gas-to-liquid transformation upon equilibrium cooling may coalesce with the neighbouring droplets to form bigger alloy droplets, contributing to the broadening in the size-distribution (detailed in section 3.4).

The composition change within these droplets can only be brought in by the long-range diffusion in the liquid phase, which also manifests in their solid particulate microstructure. Irrespective of whether the condensate is a product of equilibrium or non-equilibrium cooling, the fast-moving condensates tend to coalesce to reduce their surface free energy. In the condensed forms, the diffusion complemented by the size-effect plays a major role in deciding the compositions of the nano-droplets and nanoparticles for a very short duration as the particle formation takes place almost instantaneously. However, it is very pragmatic to infer that the composition deciding size-dependent diffusion is of long-range in the droplets whereas it is of short-range in the nanoparticles cooling down to the room temperature. Upon solidification, the alloy nanoparticles tend to coagulate and densify, the extent of which depends on their kinetic energy. The nucleation rate here in this formalism is assumed to be homogeneous and the growth rate is assumed to be comparatively prevailing more in gaseous and liquid phases whereas it is infinitesimal in the solid phase as the solidified nanoparticles only tend to coagulate and densify. The sequence of phase transformations, energetics, kinetics and size-dependent thermodynamics involved are elaborated in this section and the **Fig. 3**. schematically describes the alloy nanoparticle formation mechanism according to the proposed formalism. The driving force for the nanoparticle formation is derived from the tendency of the gaseous mixture to reduce its Gibbs free energy. When the alloy wire is exploded, the binary gaseous mixture of Al and Mg metallic vapours is formed due to Brownian motion. The repeated collisions among the constituent species produce the product molecules which nucleate upon supersaturation, grow

and form surfaces to reduce the free energy of the system, eventually resulting in the formation of alloy nanoparticles.

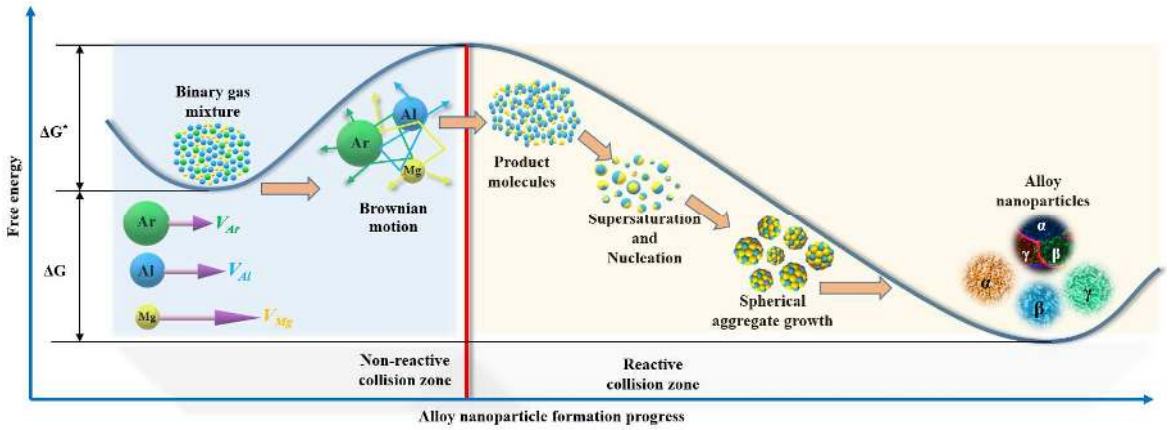


**Fig. 3**. Formation mechanism of alloy nanoparticles in wire explosion.

### 3.1 Hume-Rothery Conditions for Alloy Nanoparticles

An alloy is a mixture of two or more metallic elements, which can either exhibit single-phase characteristics existing as a complete solid solution or exhibit two or more phases existing as a phase-segregated or partial solid solution. Hume-Rothery rules describe the conditions that govern the dissolution of an element in a bulk metal forming an alloy. The rules suggest the alloy can be formed if the atomic radius, valency and electronegativity of the constituent elements are closely similar and they share a common crystal structure [44]. Extensive substitutional solid solubility occurs when the relative difference between the atomic radii of the constituent species is less than 15%. Intermetallic compounds are likely to result instead of a binary substitutional solid solution if one element is more electropositive and the other one is more electronegative. But these rules are valid for the bulk materials and have been widely used since their proposal in the 1930s. The geometrical shape of the alloy nanoparticles is normally very different from their bulk crystal structure, and similar differences can be observed in the electronic structure of ultra-fine particles relative to their bulk. **Fig. 4**. shows the comparison of Al and Mg in terms of their atomic size ($r$), electronegativity ($\chi$) and bond dissociation energy ($\Phi$). The two dimensional projected graph of electronegativity versus atomic radius within the figure is called the Darken-Gurry plot [45] which shows the Darken-Gurry ellipses of Al and Mg in this domain. A variation of ±15% in terms of atomic radius and a variation of ±5% in terms of electronegativity, centred on the absolute values, are considered in drawing these ellipses. The ellipses coincide with each other for an isomorphous alloy system whereas they tend to move apart as the solid solubility of the alloy system decreases. Ken Miyajima et al. reported that the Hume-Rothery rules do not apply to the sub-nanometer alloy clusters [46]. In the WET method, when the alloy wire is exploded, the constituent elements sublimate and form a chaotic gaseous

mixture wherein the alloying reactive collisions are probabilistic which leads to the formation of the product phases that deviate from the absolute stoichiometry and the equilibrium phases predicted by conventional phase diagrams. Al has a face-centred cubic (FCC) crystal structure and Mg has a hexagonal close-packed crystal structure which violates the first Hume-Rothery condition of common crystal structure and hence fails to exhibit extensive solid solubility of Mg in Al. Mg is an s-block, group-2 alkaline earth metal which has a valence number 2 and Al is a p-block, group-13 post-transition metal which has a valence number 3 [47]. This difference in valence numbers violates the valency rule, reducing the substitutional solid solubility further. Also, the Al-Mg alloy system violates the rule of electronegativity as Mg and Al possess the electronegativity values 1.31 and 1.61, respectively. On the contrary, there exists only an 11.8% difference between the atomic radii of Al and Mg which is within the limit of 15% difference. The partially overlapping ranges of atomic radii in the Darken-Gurry ellipses of Al and Mg as shown in **Fig. 4**. indicate the possible range of substitutional solid solubility. In addition to this favourable atomic size difference, the gas-phase reactions and the size effects enhance the solid solubility of the alloy system.

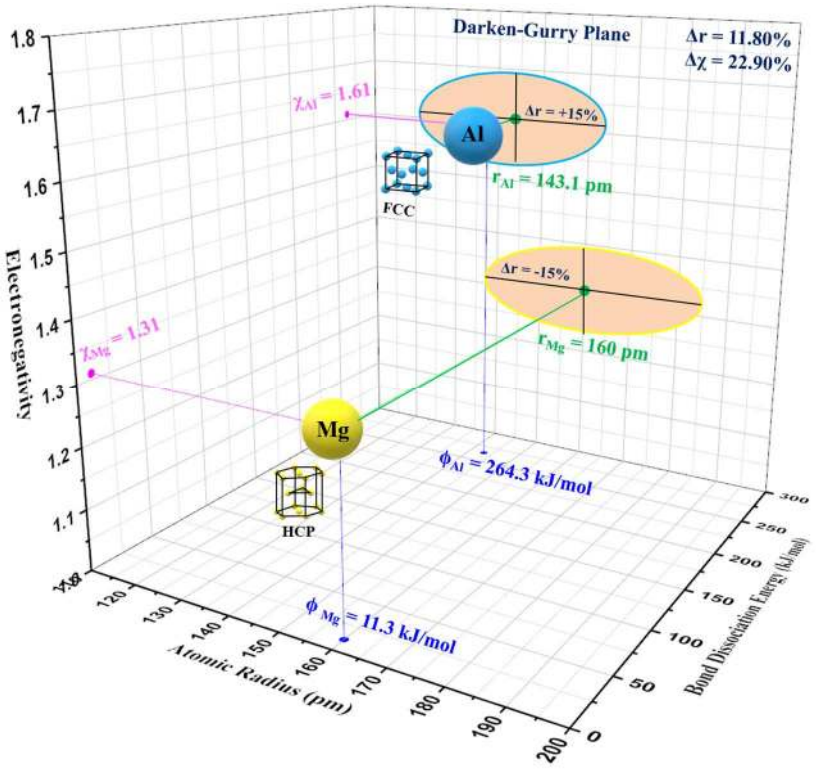


**Fig. 4**. Comparison of Al and Mg using Darken-Gurry plot and their bond dissociation energies.

### 3.2 Gas-phase Kinetics

The gas-phase reactions begin as soon as the alloy wire sublimates into its constituent gaseous species and the extent of binary product gas formation depends on the kinetic energy of the reactive atoms in the binary gas. **Fig. 5**. shows the high-speed imaging of the eutectic Al-Mg alloy wire-explosion phenomenon inside the sapphire explosion chamber from the instant of triggering for a few microseconds. The melting temperatures of Al and Mg are 933 and 923K respectively and their vapour pressures are $3.06 \times 10^{-13}$ and $21.5 \times 10^{-3}$ kPa correspondingly, at 800K [48]. The expression for the evaporation rate is described by **Eq. (4)** [49]:

$$w = 1.574 \theta P \sqrt{\frac{M}{T}} \tag{4}$$

where $P$ is the vapour pressure, $\theta$ is the condensation constant of the metal, $M$ is the molecular mass of the gas and $T$ is the temperature. It is evident from the **Eq. (4)** that the vapour pressure of the metal dominantly affects the evaporation rate at a constant temperature. At any temperature, the vapour pressure of Mg is around $10^7$ times higher than that of Al [50] as a consequence of which the evaporation rate of Mg is much higher than that of Al. It implies that the cloud of Mg is formed before the gaseous Al cloud is formed inside the explosion chamber.

All the constituent gases inside the explosion chamber are assumed to be perfect gases consisting of molecules in the form of solid spheres with ceaseless random motion. It follows that the gas molecules at a temperature $T$ move with a mean speed of $\bar{v}$ which is given as

$$\bar{v} = \sqrt{\frac{8RT}{\pi M}} \tag{5}$$

where $R$=8.3145 J/(mol-K) and the individual molecular speeds ($v$) span a wide range following the Maxwell distribution which is given as

$$f(v) = 4\pi \left( \frac{M}{2\pi RT} \right)^{3/2} v^2 \exp\left( -\frac{Mv^2}{2RT} \right) \tag{6}$$

When the alloy wire is sublimated, a binary mixture of Al and Mg gases is formed within the inert Ar gas. The molecular masses of Mg ($M_{Mg}$= 24.31 g/mol), Al ($M_{Al}$= 26.98 g/mol) and Ar ($M_{Ar}$= 39.95 g/mol) are such that $M_{Mg} < M_{Al} < M_{Ar}$. As depicted by **Eq. (5)**. the lighter molecules travel faster than the heavier molecules and hence in the ternary gaseous mixture Ar molecules travel at the slowest speed and Mg molecules travel at the highest speed. In addition to being the heaviest molecule in the system, Ar being an inert gas does not involve in any reactive collisions and just acts as a background gas. Hence, it is judicious to infer that the activation energy for the reactive collisions with Ar is infinitely high and the collisions of Al and Mg molecules with Ar will only alter their momenta and not the chemical state. More details on the reactive gas-phase kinetics are provided in the Supplementary Material and collectively from **Eq. (A.2)** and **Eq. (A.5)** it can be computationally inferred that the lower explosion pressures favour very fine particle-size owing to the reduced collision flux and

increased mean free-path at low pressures and the correlation among them is a shown in **Fig. 6**. Extending this equivalence to the wire explosion deduces that the particles formed away from the central dense plasma are comparatively finer compared to those formed in the core of the plasma. If the plasma is allowed to expand to larger volumes, even finer particles can be produced as the cooling rate increases towards the periphery of the explosion chamber.

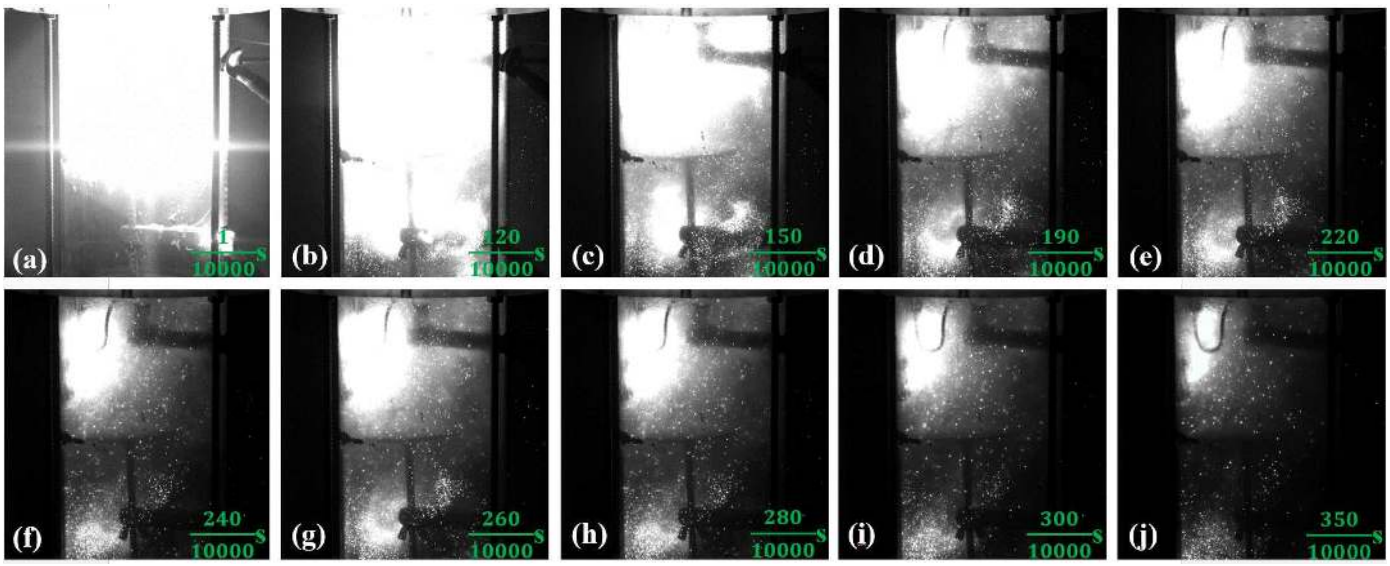


**Fig. 5.** High-speed imaging of the Al-Mg alloy-wire explosion process inside the sapphire explosion chamber in the sequence of a-j.

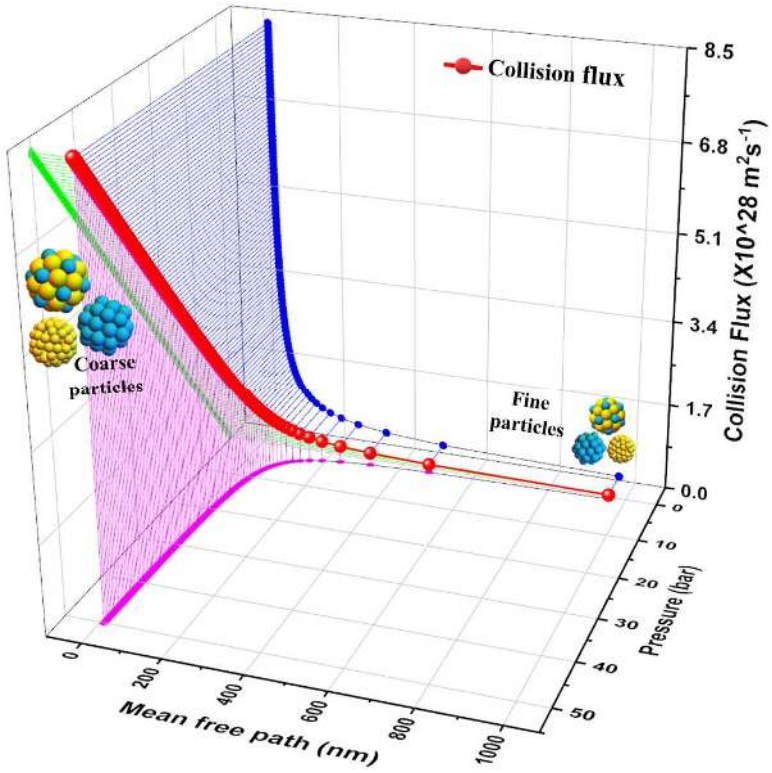


**Fig. 6.** Effect of explosion pressure, mean free-path and collision flux on Al-Mg alloy nanoparticle size.

### 3.3 Embedded Atom Method Analysis of Alloy Nanoparticles:

When two reactive species in the gaseous phase collide with sufficient energy at appropriate steric angles, they pair-up forming bonds positioning themselves at the equilibrium distance. When observed atomistically, the positioning and pairing up are the consequence of potential energy minimization and hence this process of atom embedding in the resultant product molecules needs an atomistic explanation. Here in this work, we employ the embedded atom method (EAM) for explaining the equilibrium placement of binary alloy pairs. In this methodology, each solute atom is viewed as an impurity in the electron cloud of the host solvent. The embedding energy required to embed a solute atom (Mg) in a solvent (Al) is used to determine the cohesive energy of the solid alloy as the energy of the solute impurity atom is a function of the electron density of the host solvent. The Lennard-Jones (L-J) pair-potential function is adopted here for the minimization of potential energy. To account for the large surface area of the nanoparticles, the cohesive energy is made size-dependent [51] as shown in Eq. (19). The term d/D accounts for the size-reduction and hence the surface area increased upon introducing new dangling bonds in the nanoparticle. The EAM framework is graphically demonstrated in **Fig. 7**. along with the L-J potential for the Al-Al, Mg-Mg and Al-Mg pairs. The cohesive energy of a binary alloy nanoparticle according to EAM is the sum of embedding energy and the pair-potential and is written as [52]

$$E_{coh} = \sum_i F_i(\rho_i) + \frac{1}{2}\sum_{\substack{i,j \\ i \neq j}} \phi_{ij}(R_{ij}) \tag{7}$$

where $F_i$ is the embedding energy of the individual atom, $\rho_i$ is the electron density of the solvent at the position $R_i$, $R_{ij}$ is the distance between the atoms i and j and $\phi_{ij}$ is the short-range pair potential between them. The L-J pair potential of interatomic interaction is described by the following expression

$$\phi_{ij}(r) = 4\varepsilon_{ij}\left[\left(\frac{r_0}{r}\right)_{ij}^{12} - \left(\frac{r_0}{r}\right)_{ij}^{2}\right] \tag{8}$$

where the potential parameters are $\varepsilon_{Al-Al}$=0.50722eV, $\varepsilon_{Mg-Mg}$=0.0958eV, $\varepsilon_{Al-Mg}$=0.2204eV and $r_{ij}$ is the distance between the atomic centres [53]. The equilibrium distances for Al, Mg and Al-Mg binary alloy are found to be $(r_0)_{Al\text{-}Al}$=2.57366Å, $(r_0)_{Mg\text{-}Mg}$=2.88Å and $(r_0)_{Al\text{-}Mg}$=2.7268Å, respectively, as shown in **Fig. 7**. It is evident from the figure that the equilibrium separation for the Al-Mg binary eutectic alloy is intermediate between that of Al-Al and Mg-Mg pairs satisfying the Vegard's law [54] which states that the effective lattice parameter of a solid solution varies directly and almost linearly with the solute concentration, as a weighted average of the lattice spacing of the solvent and solute.

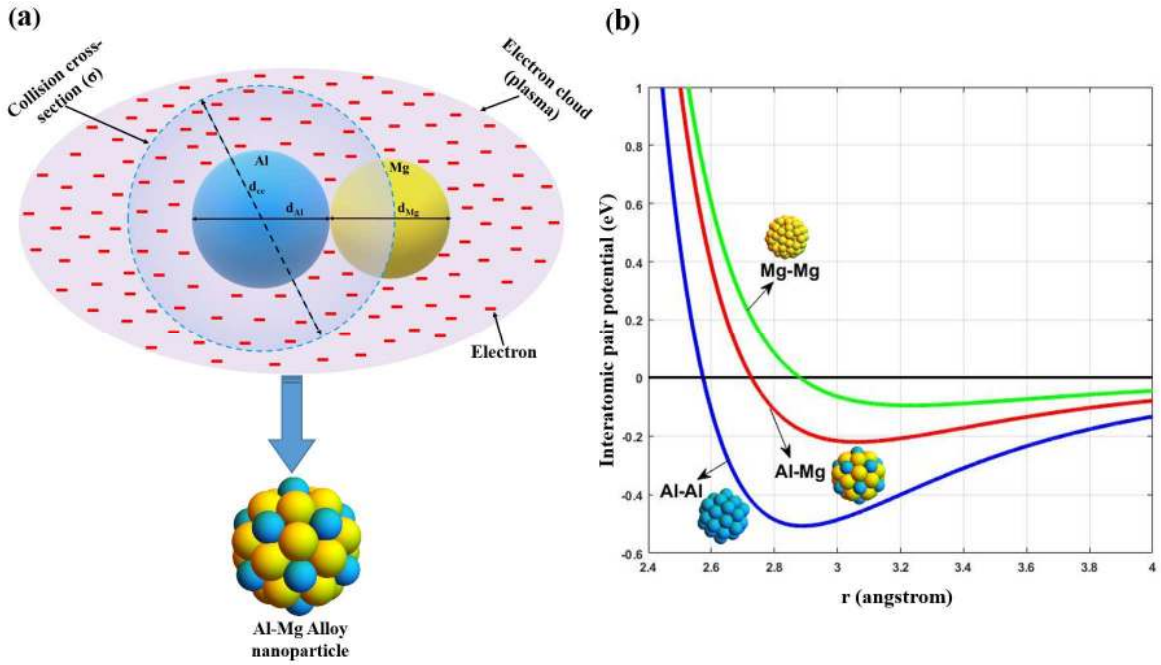


**Fig. 7.** (a) Schematic of EAM model and (b) Lennard-Jones interatomic interaction potential for Al-Al, Mg-Mg and Al-Mg pairs.

### 3.4 Equilibrium and Non-Equilibrium Phase Transformations:

A majority of the product forming reactions take place in the gaseous phase in the binary alloy nanoparticle synthesis through the WET. As aforementioned, the products of the reactive collisions will undergo phase transformation upon supersaturation. Now that the gaseous mixture senses a temperature gradient between itself and the external ambient temperature, it tends to reduce its free energy by undergoing phase change either through equilibrium or non-equilibrium cooling. In both the cases of cooling, the formation of a new phase begins via formation of embryos which are transient tiny clusters with constantly fluctuating size by attachment and desorption of molecules [55]. This process of attachment and detachment makes the embryos eventually attain a stable size above which there is no size shrinkage, and result in the nucleation of the respective condensed phases (droplets and nanoparticles). Various studies confirm the presence of a small proportion of molten droplets along with the metal vapour in the dispersion products, during wire explosion [56, 57]. In case of a brass alloy, the wire does not sublimate completely into gaseous phase even with excess energy deposition [58]. Hence, it can be judiciously inferred that the possible presence of molten droplets in the explosion products can not be ruled out and in turn, these droplets can solidify either through equilibrium or non-equilibrium cooling. The nuclei formed during the solidification can grow by various mechanisms such as diffusion, oriented attachment, coagulation and coalescence. The process of nucleation is detailed in the Supplementary Material.

A sequence of processes occurs in the liquid to solid transformation with a characteristic difference of phase boundary formation between the parent liquid and the new solid phase to reduce the surface energy. Owing to the high-temperature state of alloy droplets, the diffusion plays a major role in the growth of droplets as it is size-dependent in addition to being temperature-dependent. For a compositionally homogeneous alloy nanoparticle, the expression for the size-dependent heat of formation ( $E_{f,d}^{Al-Mg}$ ) as a function of cohesive energy of constituent elements can be written as

$$E_{f,d}^{Al-Mg} = E_{c,d}^{Al-Mg} - \left[(1-x)E_{c,d}^{Al} + xE_{c,d}^{Mg}\right] \tag{9}$$

where $E_{c,d}^{Al}$, $E_{c,d}^{Mg}$ and $E_{c,d}^{Al-Mg}$ are the corresponding size-dependent cohesive energies of Al, Mg and Al-Mg. The size-dependent cohesive energy ( $E_{c,d}^{i}$ ) is written as [59]

$$E_{c,d}^{i} = E_{c,b}^{i}\left(1-3\alpha^{i}\frac{d}{D}\right) \tag{10}$$

where $E_{c,b}^{i}$ is the bulk cohesive energy of the i$^{th}$ constituent element, $d$ is the atomic size, $D$ is the nanoparticle size and $d/D=(1/N)^{1/3}$ in which $N$ is the total number of atoms in the nanoparticle. Based on **Eq. (9)** and **Eq. (10)** the expression for size-dependent, shape-dependent and composition-dependent formation enthalpy of a homogeneous disordered solid solution of Al-Mg alloy system can be written as

$$E_{f,d}^{Al-Mg} = E_{c,b}^{Al-Mg}\left(1-3\alpha^{Al-Mg}\sqrt[3]{\frac{1}{N}}\right) - \left[\begin{array}{l}\left\{(1-x)3\alpha^{Al}E_{c,b}^{Al}\left(1-3\sqrt[3]{\frac{1}{N(1-x)}}\right)\right\}+ \\ \left\{x3\alpha^{Mg}E_{c,b}^{Mg}\left(1-3\sqrt[3]{\frac{1}{Nx}}\right)\right\}\end{array}\right] \tag{11}$$

where is $\alpha^{i}$ the shape factor and is equal to unity for spherical nanoparticles. The cohesive energy of the Al-Mg eutectic alloy with disorder solid solution can be computed using the EAM potential as

$$E_{c,b}^{Al-Mg} = (1-x)\left[\frac{1}{2}\phi^{Al}(r)+F^{Al}(\rho)\right]+x\left[\frac{1}{2}\phi^{Mg}(r)+F^{Mg}(\rho)\right] \tag{12}$$

where $\phi^{i}$ is the pair-potential and $F^{i}$ is the embedding energy. It is evident from the computational analysis of **Eq. (11)** that the formation enthalpy decreases with the alloy nanoparticle size as shown in **Fig. 8**. In addition to this, the Al-Mg alloy system did not exhibit any positive formation enthalpies throughout the entire composition range which indicates that there is no miscibility gap or spinodal-decomposition zones.

The Al-Mg alloy system is a dual binary-eutectic exhibiting two eutectic points one of which is Al-rich and the other is Mg-rich. The chosen eutectic alloy in the present work is Al-

rich as it is more ductile in comparison with the Mg-rich brittle-eutectic and this makes the fabrication of thin alloy wires through EDM easy. An earlier work of our group demonstrated that addition of nano-aluminium to the solid rocket propellants increases the burning rate and hence the specific impulse of the rocket motor by around 15% [60] and Mg powders burn faster than the Al powders of similar size [10]. Hence, the addition of Mg to Al in eutectic proportion is likely to enhance the burning rate further and reduce the ignition temperature and delay. **Fig. 9a.** shows the equilibrium phase diagram of the Al-rich eutectic is in which the Al-rich eutectic temperature ($T_E$) is 450$^0$C and the green lines within the phase-boundaries are tie-lines connecting the compositions of the phases in equilibrium at respective temperatures. The phase diagram calculation is performed using the commercially available ThermoCalc software and according to the experimentally calculated phase diagram [61] the eutectic reaction for the alloy system can be written as

$$\mathbf{L}\ (34.45\ \text{wt\% Mg}) \xrightleftharpoons{450^0\text{C}} \boldsymbol{\alpha}\ (17.07\ \text{wt\% Mg}) + \mathbf{Mg_{28}Al_{45}}\ (35.57\ \text{wt\% Mg}) \qquad (13)$$

The α-phase is a solid solution rich in Al with Mg as the solute and has an FCC crystal structure. The $Mg_{28}Al_{45}$ phase is rich in Mg compared to the α-phase and the region below the tie-line at $T_E$ =450$^0$C is a dual-phase solid region where both α and the $Mg_{28}Al_{45}$ phases coexist together in the microstructure. The significance of the eutectic reaction is that, similar to the solidification of pure substances, the reaction proceeds to completion isothermally upon cooling.

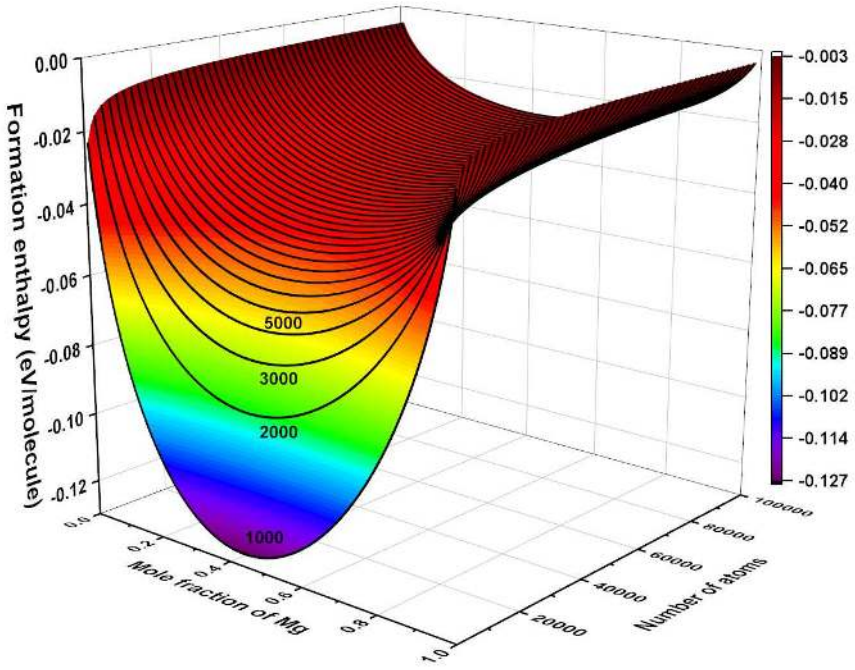


**Fig. 8.** Size-dependent formation enthalpy of the Al-Mg alloy nanoparticles.

The phases depicted by the phase diagram are the equilibrium phases whereas the solid phases that form upon wire explosion follow non-equilibrium cooling due to excess

energy deposition and hence tend to deviate from the equilibrium phases. As shown in Fig. 9(a) by the equilibrium cooling curve, the first condensed phase that forms is a liquid phase containing both Al and Mg, above the liquidus. These minuscule droplets of the liquid phase grow with the adsorption and diffusion of gaseous molecules at higher temperatures whereas they grow with the coalescence of droplets and adsorption of diffusing gaseous molecules at lower temperatures. Hence, the nanoparticle growth occurs predominantly in the liquid phase in equilibrium cooling as opposed to the non-equilibrium quenching wherein the nanoparticles grow by sintering, coagulation and oriented attachment of the solidified nanoparticles. The ephemeral liquid phase growth continues until the droplet temperature reaches the eutectic temperature and seizes to grow by adsorption and diffusion below $T_E$.

The eutectic point in the Al-rich portion of the phase diagram is a triple point where three phases liquid (L), Al-rich solid solution (α) and $Mg_{28}Al_{45}$ coexist and their equilibrium coexistence is predicted with the thermodynamically computed Gibbs free energy curves at $T_E$ as shown in **Fig. 9(b)**. The common tangent drawn in the Gibbs free energy plot connects all the three coexisting equilibrium phases at $T_E$ with all the three equilibrium composition points collinear on the common tangent. However, as the quenching of nanoparticles is a transient and non-equilibrium process, the synthesized nanoparticles are likely to deviate from the equilibrium dual-phase microstructure and composition. As indicated in Fig. 9(a), the rapid quenching (non-equilibrium) process bypasses the intermediate liquid phase as opposed to the slow (equilibrium) cooling due to extreme temperature gradients.

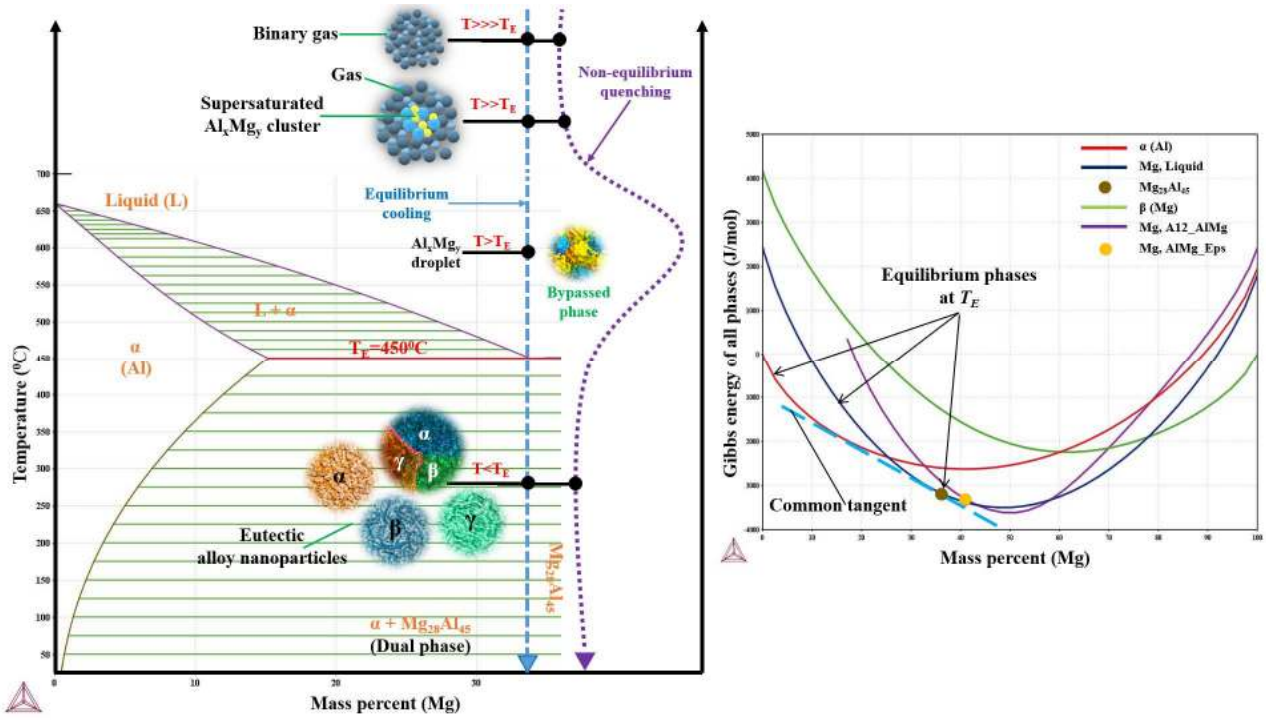


**Fig. 9.** (a) Computed Al-rich eutectic portion of the Al-Mg alloy phase diagram (b) corresponding Gibbs free energy of various phases present in the Al-Mg equilibrium phase diagram at the eutectic temperature $T_E$.

### 3.4.1 Size-dependent Thermodynamic Description of Eutectic Al-Mg Alloy Nanoparticles

The physicochemical properties of small systems such as alloy nanoparticles, greatly differ from their bulk counterparts due to their high surface area and hence excess surface free energy. The solidus and liquidus temperatures of the alloy system drop as a result of size-effect which consequently decreases the area of two-phase zones in the phase diagram [62]. This necessitates the need for understanding the nanoscopic alloy systems and examine the size-induced changes in their physicochemical characteristics. At constant $T$ and $P$, incorporating the surface energy, the expression for Gibbs free energy of a small system can be written in the differential form as

$$dG = VdP - SdT + \sum_i \mu_i dn_i + \gamma dA \tag{14}$$

where $S$ is the entropy, $V$ is the volume, $\mu_i$ is the chemical potential of component $i$, $n_i$ is the number of species $i$, $A$ is the surface area and $\gamma$ is the surface energy. For a small spherical system of surface area $A$ and volume $V$,

$$dA = \frac{2}{r}\sum_i V_i dn_i \tag{15}$$

A detailed description of the size-dependent thermodynamics of Al-Mg binary eutectic system can be found in the Supplementary Material. The size-effect influences the free energy of the equilibrium phases in such a way that it decreases their liquidus and solidus temperatures consequently reducing the dual-phase region. These alterations in the phase boundaries will eventually change the eutectic composition and the resulting equilibrium phases. Hence, it is very practical to anticipate deviated stoichiometry in the alloy nanoparticles produced by the explosion of Al-Mg alloy wire.

### 3.4.2 Growth, Coalescence and Coagulation

Along with the phase transformations, starting from the gas phase until the alloy nanoparticle formation, the diffusion process proceeds in parallel accounting for the nucleation and growth of the resultant gas and condensed phase products. In addition to the diffusion process, the diffusing species react with the solvent products and thereby contribute to the evolution of that phase. Hence during all the stages of phase transformations, diffusion and reaction inherently contribute to the formation and growth of the products though being transient. The Damköhler number ($D_a$) which is the ratio of reaction rate and diffusion rate, determines whether the transformation is diffusion-limited or reaction-limited. If $D_a >> 1$, then the reaction rate dominates the diffusion rate making the transformation diffusion-limited. If $D_a << 1$, the reactive species diffuse much faster than the rate at which the reaction

proceeds, in which case the transformation becomes reaction-limited. For the alloy nanoparticle growth, the Damköhler number can be written as [63]

$$D_a = \frac{RT}{2\gamma_{np,Al-Mg} V_{m,Al-Mg}} \frac{D_{Al-Mg}}{k_f} \tag{16}$$

where $\gamma_{Al\text{-}Mg}$ is the surface energy of the growing alloy nanoparticle, $V_{m,Al\text{-}Mg}$ is the molar volume of the $Al_xMg_y$ alloy nanoparticle, $D_{Al\text{-}Mg}$ is the diffusivity of the alloy nanoparticle and $k_f$ is the apparent reaction rate constant. The surface energy of the alloy nanoparticle can be calculated using the expression [64]

$$\gamma_{np,Al-Mg} = \left(\gamma_{Al-Mg}\right)_{SV} \left[1 - \frac{3}{4}\frac{\eta}{\rho^{2/3}} n_t^{-1/3}\right] \tag{17}$$

where $\eta$ and $\rho$ are the packing fraction parameters whose values are 0.74 and 0.9 respectively, $n_t$ is the total numbers of atoms in the alloy nanoparticle and $\left(\gamma_{Al-Mg}\right)_{SV}$ is the surface energy of the Al-Mg binary alloy, which is described in the Supplementary Material.

For the diffusion-limited growth, the growth rate $(dr/dt)_{Diffusion}$ of the alloy nanoparticle is given as

$$\left(\frac{dr}{dt}\right)_{Diffusion} = \frac{D_{Al-Mg} V_{m,Al-Mg}}{r}\left(C_{bulk} - C_r\right) = \frac{2D_{Al-Mg}\gamma_{Al-Mg} V_{m,Al-Mg}^2 C_{bulk}}{k_B T}\frac{1}{r}\left(\frac{1}{r^*} - \frac{1}{r}\right) \tag{18}$$

where $C_{bulk}$ is the bulk concentration of the alloy monomer within the parent phase and $C_r$ is the solubility of the Al-Mg nanoparticle. The diffusivity $D_{Al-Mg}$ of alloy nanoparticles can be determined by using Darken's equation: $D_{Al\text{-}Mg}=x_{Al}D_{Mg}+x_{Mg}D_{Al}$.

Apart from the limitations imposed by diffusion, the growth could also be limited by the interface adsorption in which case the growth rate is [65]

$$\left(\frac{dr}{dt}\right)_{Adsorption} = k_f V_{m,Al-Mg}\left(C_{bulk} - C_r\right) = = \frac{2k_f \gamma_{Al-Mg} V_{m,Al-Mg}^2 C_{bulk}}{k_B T}\left(\frac{1}{r^*} - \frac{1}{r}\right) \tag{19}$$

When the particle size ($r$) is less than the critical size ($r^*$), the growth rate according to the **Eq. (18)** and **Eq. (19),** the diffusional and adsorptive growth rates respectively become negative which in the physical sense the alloy cluster dissolves as it is not stabilized its size to grow further. In the diffusion-controlled growth, the cluster with a size more than $r^*$ will continue to grow and culminates with a maximum growth rate when the cluster size is $2r^*$. Until the size of $2r^*$, the larger particles grow faster than the smaller particles as a consequence of which the size distribution broadens. Beyond the size $2r^*$, the growth of the particles decreases with smaller particles growing faster than the larger particles eventually resulting in the nanoparticles of uniform size and growth rate. Hence, diffusion-controlled growth results in the formation of nearly monodispersed nanoparticles. In the adsorption-controlled growth, the larger nanoparticles always grow faster than the smaller particles resulting in the polydispersed nanoparticles. The computational results of diffusional and

adsorption growth rates of a hypothetical 5 nm Al-Mg alloy nanoparticle and the respective mechanisms are shown in **Fig. 10**.

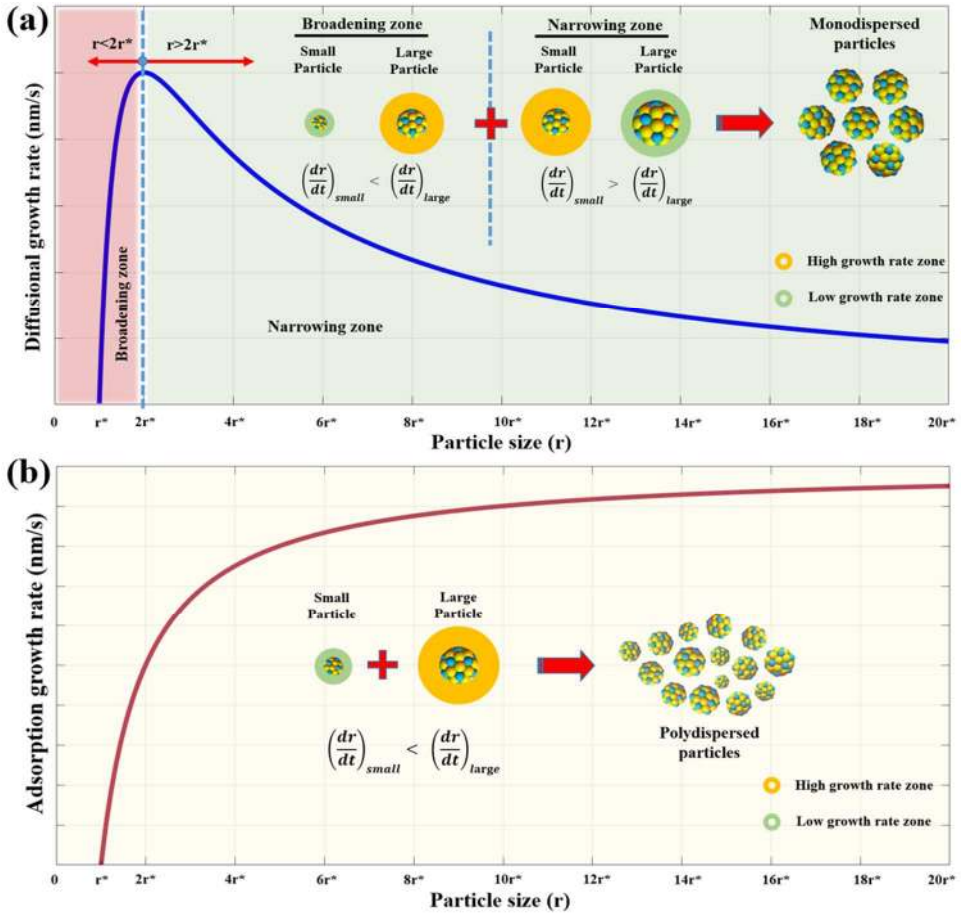


**Fig. 10.** Size-dependent (a) diffusional growth and (b) adsorption growth of Al-Mg alloy nanoparticles.

In addition to the kinetic parameters of formation and growth, the post-formation and growth parameters such as coalescence and coagulation also influence the mean particle size and the distribution of the nanopowders. The rate at which the collisions and coalescences take place dictates the formation of spherical and non-spherical particles and their size in the gas-phase synthesis of nanoparticles. According to the solid-state diffusion model, the characteristic coalescence time ($\tau_{coalsescence}$) is written as [66]

$$\tau_{coalescence} = \frac{3k_B T_p N}{64\pi\gamma D} \tag{20}$$

where $D$ is the coefficient of diffusion, $\gamma$ is the surface tension, $N$ is the total number of atoms in the particle and $T_p$ is the particle temperature. The collision time ($\tau_{collision}$) according to the kinetic theory of gases is written as

$$\tau_{collision} = \frac{\sigma P \bar{c}_{rel}}{k_B T} \tag{21}$$

where $\sigma$ is the collision cross-section of the alloy particle. At higher temperature, the rate of coalescence is more than the rate of collision i.e., $\tau_{coalsescence} < \tau_{collision}$ which results in the spherical nanoparticles. However, at a lower temperature, particle coalescence kinetics is very sluggish i.e., $\tau_{coalsescence} > \tau_{collision}$ which produces non-spherical agglomerates.

## 4. Results and Discussion

### 4.1 Structural Characterisation

The process of synthesizing eutectic alloy nanoparticles began with the Al-Mg eutectic alloy wire cut using the EDM technique. The eutectic composition of the alloy wire was confirmed by inductively coupled plasma optical emission spectrometry (ICP-OES). The EDM cut alloy wire was homogenized for 50 hours at $0.5T_m$=225$^0$C in the furnace before the X-ray diffraction studies and microstructural analysis. **Fig. 11.** shows the X-ray diffractogram of the homogenized alloy wire from which it is clear that the eutectic material contained a crystalline dual-phase. Al-Mg equilibrium phase diagram as shown in **Fig. 9.** depicted that the eutectic alloy of 34.55 wt% Mg consists of an Al-rich solid solution and an intermediate solid-phase $Mg_{28}Al_{45}$. The diffractograms are indexed by using X'pert HighScore Plus software. The X-ray diffractogram confirms the presence of an Al-rich solid solution $Al_{3.7}Mg_{0.3}$ FCC phase which exhibited the most intense peak at 2θ=38.155$^0$. The other crystalline phase predicted is $Al_{3.11}Mg_2$ with its most intense peak at 2θ=35.951$^0$ whose Al/Mg atomic ratio is 1.555 which is marginally deviated from the ratio 1.607 as predicted by the equilibrium phase diagram.

The alloy wire sample was polished and etched with Keller's reagent to observe the microstructure under the light and scanning electron microscopes. The alloy exhibited the typical dendritic microstructure when observed under the light microscope as shown in **Fig. 12(a).** which is a characteristic eutectic microstructure. The scanning electron microscopy (SEM) of the same sample revealed the clear dendritic two-phase microstructure as shown in **Fig. 12(b)**. The EDX analysis confirmed the presence of two distinct Al-rich phases with different Al and Mg concentrations as shown in **Fig. 12(c)** and **(d)**. The dendritic structures are found to contain 81.08 at% Al whereas the matrix is found to have 62.81 at% Al. Traces of oxygen is also observed as Al and Mg are very reactive and oxidize upon their exposure to the atmosphere.

The homogenized eutectic alloy wires were exploded using the wire explosion technique in presence of Ar and He ambience inside the explosion chamber at a pressure of 25 kPa to synthesize the alloy nanoparticles. The synthesized nanoparticles were analysed by X-ray diffraction studies to predict the various phases present and found three distinct crystalline phases. The X-ray diffractogram as shown in **Fig. 13**. illustrates the presence of (i) Al-rich FCC solid solution phase $Al_{3.7}Mg_{0.3}$ (ii) an intermediate $Al_{3.11}Mg_2$ phase and (iii) a

new $Al_{30}Mg_{23}$ phase with an Al/Mg atomic ratio of 1.304. The reason for the formation of the new phase and its departure from the equilibrium stoichiometry can be attributed to the non-equilibrium quenching process and the probabilistic pair-up of the components during the gas-phase reactions and subsequent phase transformations.

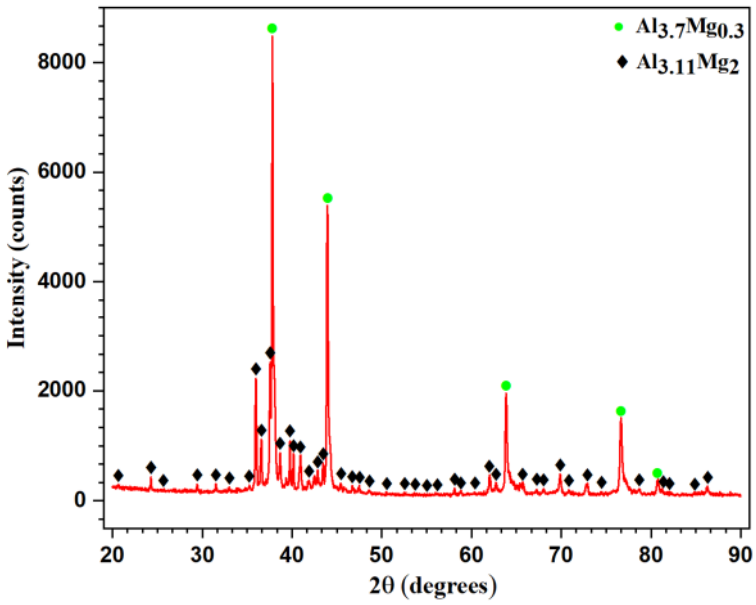


**Fig. 11.** X-ray diffractogram of the homogenized eutectic alloy wire

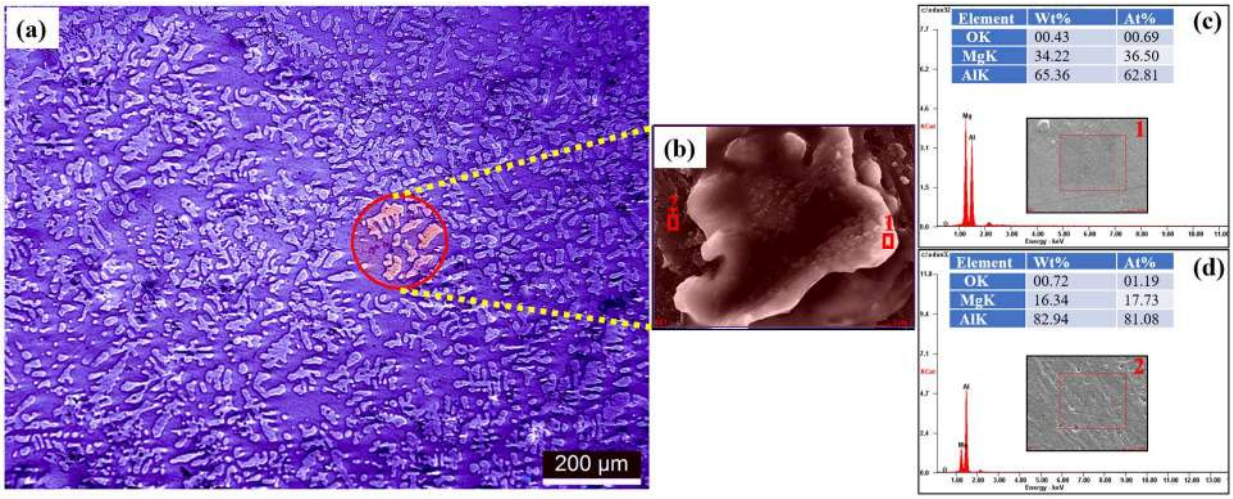


**Fig. 12.** (a) Microstructure of Al-Mg eutectic alloy wire (b) SEM of the dual-phase eutectic microstructure (c) EDAX result of the Mg-rich phase and (d) EDAX result of the Al-rich phase

The scanning electron microscopy revealed that the synthesized nanoparticles have a spherical morphology and are in the nano-size range, as shown in **Fig. 14(a)** and the EDX analysis done predicted the percentage of Al, Mg and O as shown in **Fig. 14(b)**. The presence

of oxygen is because of the reaction of Al and Mg with ambient oxygen owing to their reactive nature and increased surface area. The nanopowder area scanned for EDAX is mapped for the spatial distribution of Al and Mg in the sample as shown in **Fig. 14(c)** and confirmed the presence of Al and Mg on the surface of all the alloy nanoparticles but with a varied concentration.

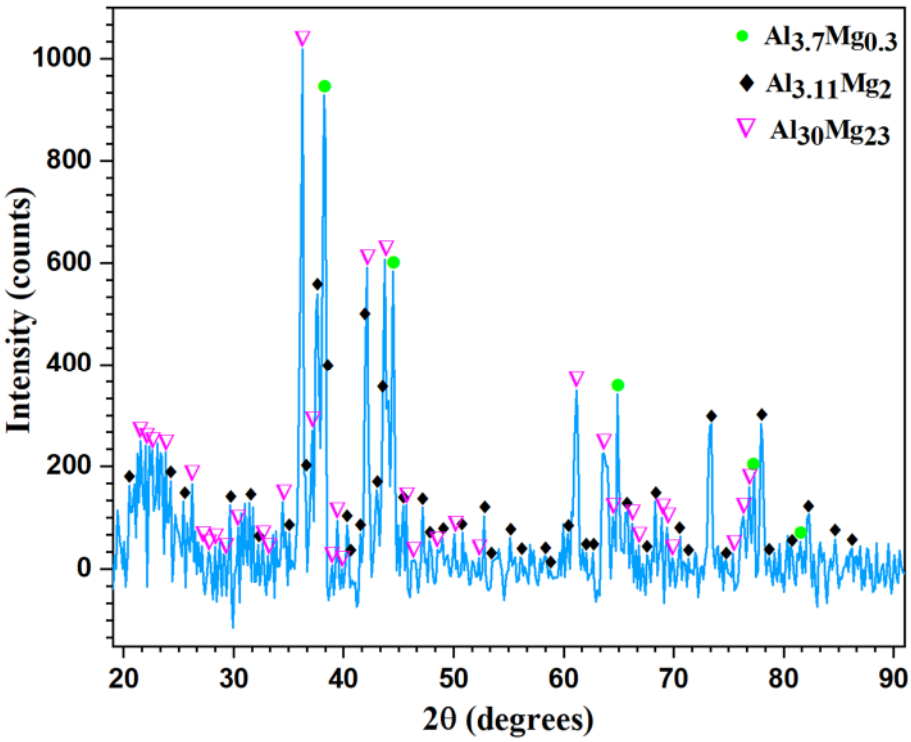


**Fig. 13.** X-ray diffractogram of the eutectic Al-Mg alloy nanoparticles.

The high-resolution transmission electron microscopic (HRTEM) study carried out confirmed that the alloy nanoparticles are multiphase and spherical as shown in **Fig. 15(a)** and **(c)** and the ring patterns observed in the selected area electron diffraction (SAED) images as shown in **Fig. 15(b)** and **(d)** substantiated that the nanoparticles are crystalline. The indexed rings revealed the presence of various atomic planes corresponding to the three distinct crystalline phases of the alloy nanopowder synthesized in both Ar and He ambiences. Also, the TEM study confirmed that the particle size distribution followed the log-normal distribution as shown in **Fig. 16**. which is written as

$$f(D) = \frac{1}{\sqrt{2\pi}\, d \log \sigma_g} \exp\left\{ -\frac{\left(\log d - \log d_{50}\right)^2}{2\left(\log \sigma_g\right)^2} \right\} \tag{22}$$

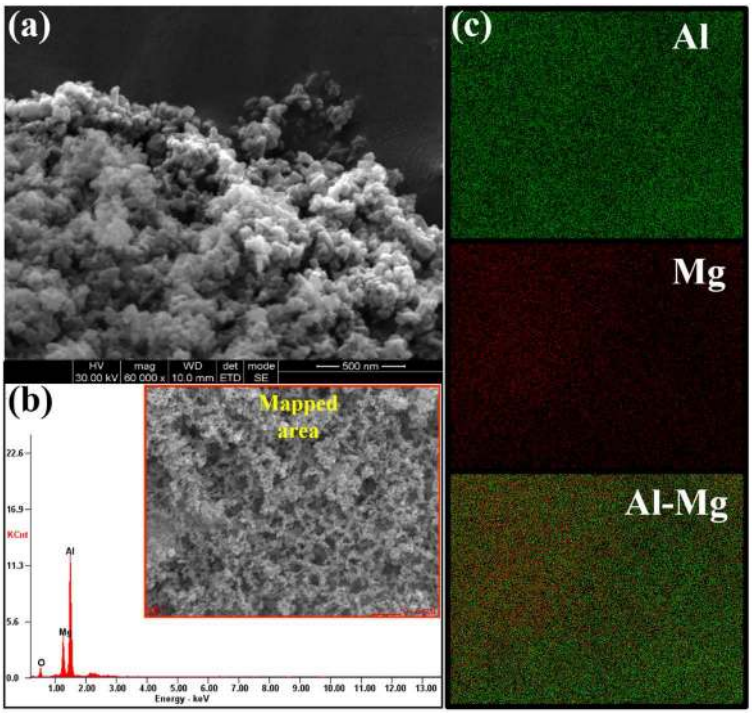


**Fig. 14.** (a) SEM micrograph of the spherical eutectic nanoparticles (b) EDAX result of the inset scanned area and (c) SEM elemental mapping of the mapped area in (b).

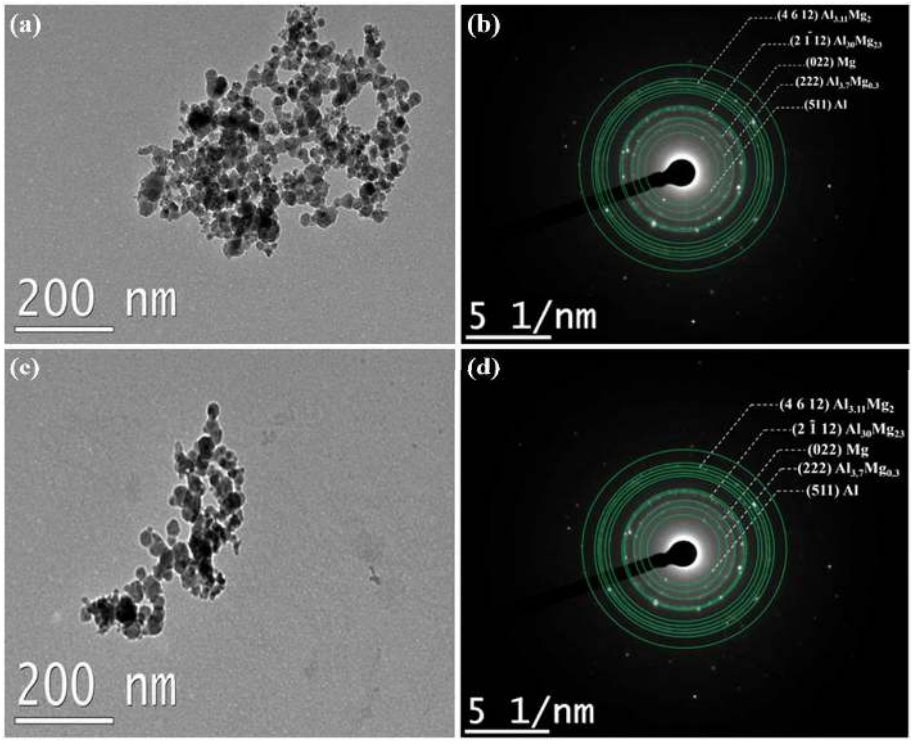


**Fig. 15.** (a) and (b) TEM micrograph and the indexed SAED pattern of the alloy nanoparticles synthesized in Ar and (c) and (d) TEM micrograph and the indexed SAED pattern of the alloy nanoparticles synthesized in He.

where $d$ is the particle diameter, $\sigma_g$ is the geometric standard deviation and $d_{50}$ is the geometric mean diameter. Then mean particle diameter is found to be around 12 nm for the nanoparticles synthesized in both Ar and He. The HRTEM elemental mapping is done to predict the spatial distribution of Al and Mg inside the alloy nanoparticles as shown in **Fig. 17**. which confirmed the distribution of Al and Mg inside the particles of the alloy nanopowder. Traces of O detected corresponds to the surface reaction of Al and Mg with O and the C mapping corresponds to the carbon layer on the TEM sample grid.

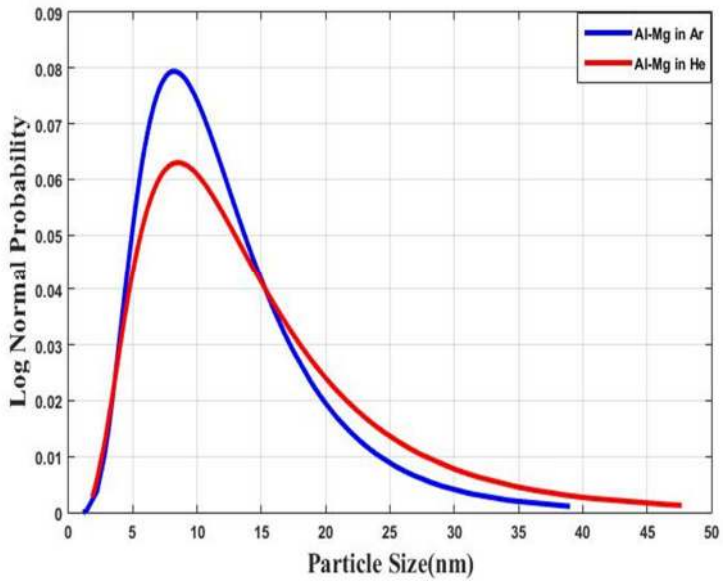


**Fig. 16.** Particle size distribution of the alloy nanoparticles synthesized in Ar and He

The scanning transmission electron microscopic (STEM) study done through the line-energy dispersive X-ray spectroscopy (line-EDS) as shown in **Fig. 18.** demonstrates the distribution of Al, Mg and O across the eutectic alloy nanoparticle that justifies the SEM and TEM elemental mapping. It is evident from **Fig. 18(b)** that the Al concentration is more than that of

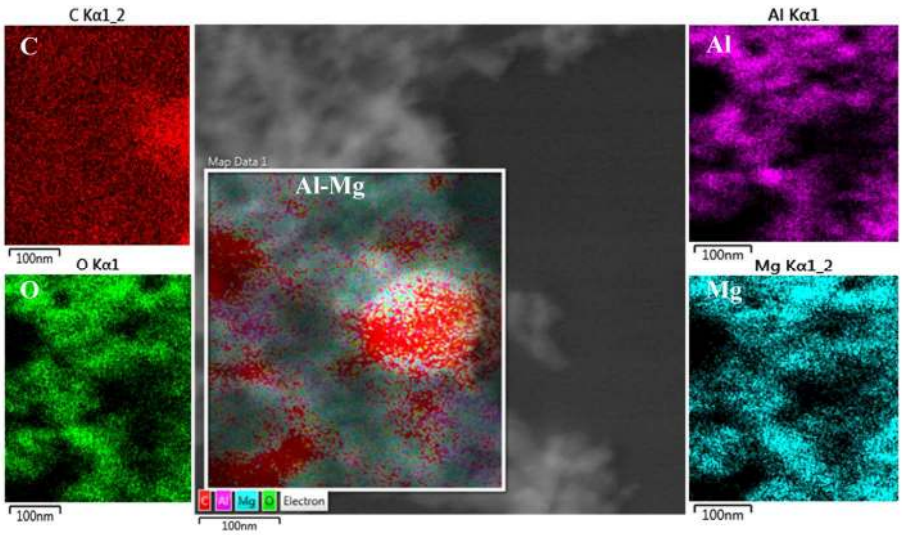


**Fig. 17.** HR-TEM elemental mapping of the synthesized Al-Mg eutectic nanoparticles

Mg across the nanoparticle which is in tandem with the phase composition predictions by the equilibrium phase diagram. Further, the HRTEM study was extended to predict the different phases present in the individual nanoparticles and the results are as shown in **Fig. (19)** and **(20)** and the alloy nanoparticles are distinctly coloured to bifurcate individual particles and to measure the interplanar distances of various phases. Two overlapping planes (266) and (177) of the same $Al_{3.11}Mg_2$ phase at an angle can be observed within a single nanoparticle from **Fig. 19(a)**. The Moire pattern is observed as a consequence of the overlapping of different atomic planes [67]. **Fig. 19(b).** shows three different nanoparticles with different phases present at inclinations within them indicating that the composition varies from one particle to another in the same nanopowder sample and the alloy particles synthesized possess multiphase microstructure. **Fig. 20.** shows the HRTEM image four nanoparticles with clearly visible atomic planes of various phases present in them confirming their crystallinity and the enlarged inset images distinct atomic planar spacing and their alignment within the nanoparticle.

### 4.2 Thermal Analysis of the Alloy Nanoparticles

The thermal analysis of the alloy nanopowder is done through the thermogravimetry-differential scanning calorimetry (TG-DSC) as shown in **Fig. 21**. This thermal signature of the Al-Mg eutectic nanopowder indicates that the melting temperature is $447.1^0$C as opposed to $450^0$C that is predicted by the phase diagram and this reduction in melting point can be attributed to the size-effect. The enthalpy of fusion is 160.2 J/g which is very low compared to that of Al (397.0 J/g) and Mg (348.9 J/g) and it can be inferred that this will tremendously reduce the ignition temperature and enhance the burning rate of the propellants embedded with Al-Mg eutectic nanoparticles. The reduction in the melting point of the metallic additives reduces the unburnt fraction in the rocket plume and leads to the formation of relatively small filigrees and agglomerates in the exhaust gases [68] which will consequently reduce the two-phase flow losses and traceability of the rocket. Also, the addition of Al-Mg alloy nanoparticles to the liquid fuels will improve the burning efficiency through nano-explosions enhancing engine performance and thereby reduces the formation of the pollutants.

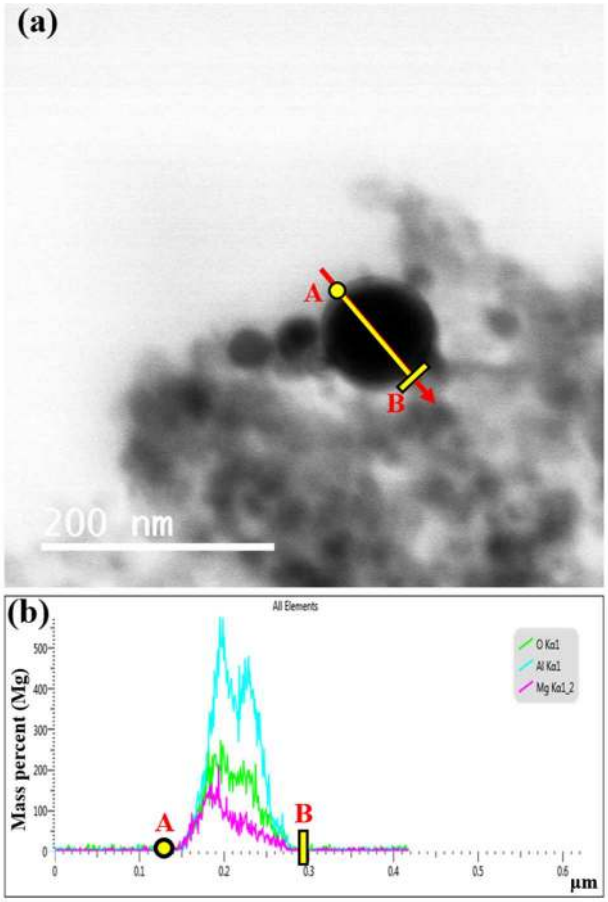


**Fig. 18.** (a) STEM micrograph and (b) line-EDS concentration profiles of Al, Mg and O in the eutectic alloy nanoparticle

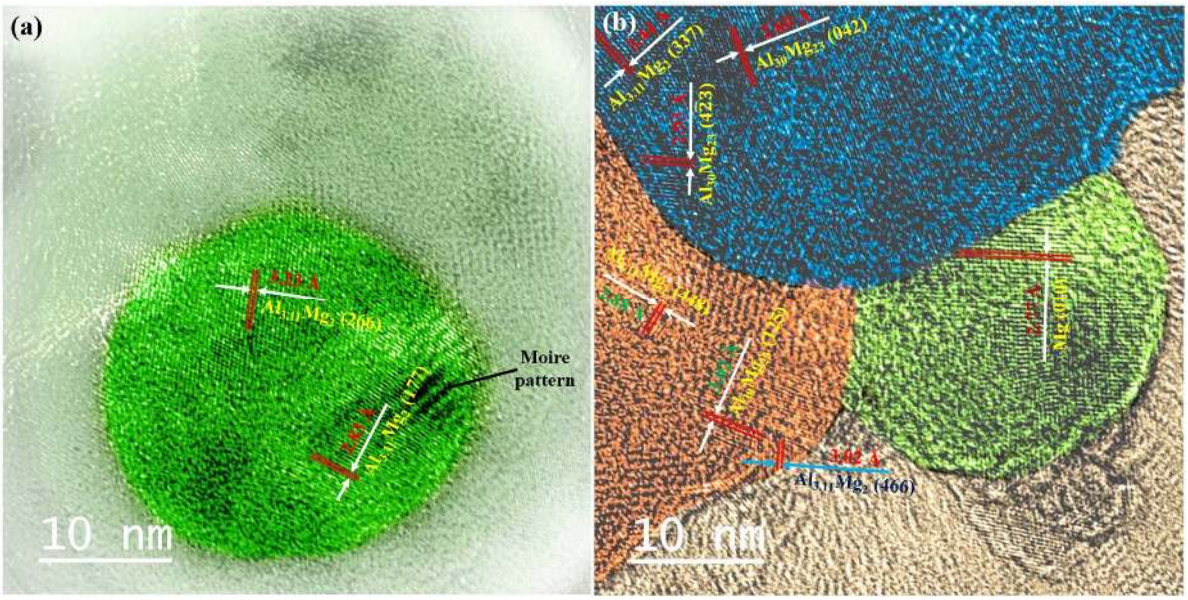


**Fig. 19.** (a) Al-Mg alloy nanoparticles with Moire patterns and (b) HR-TEM of the multi-phase alloy nanoparticles with various phases within.

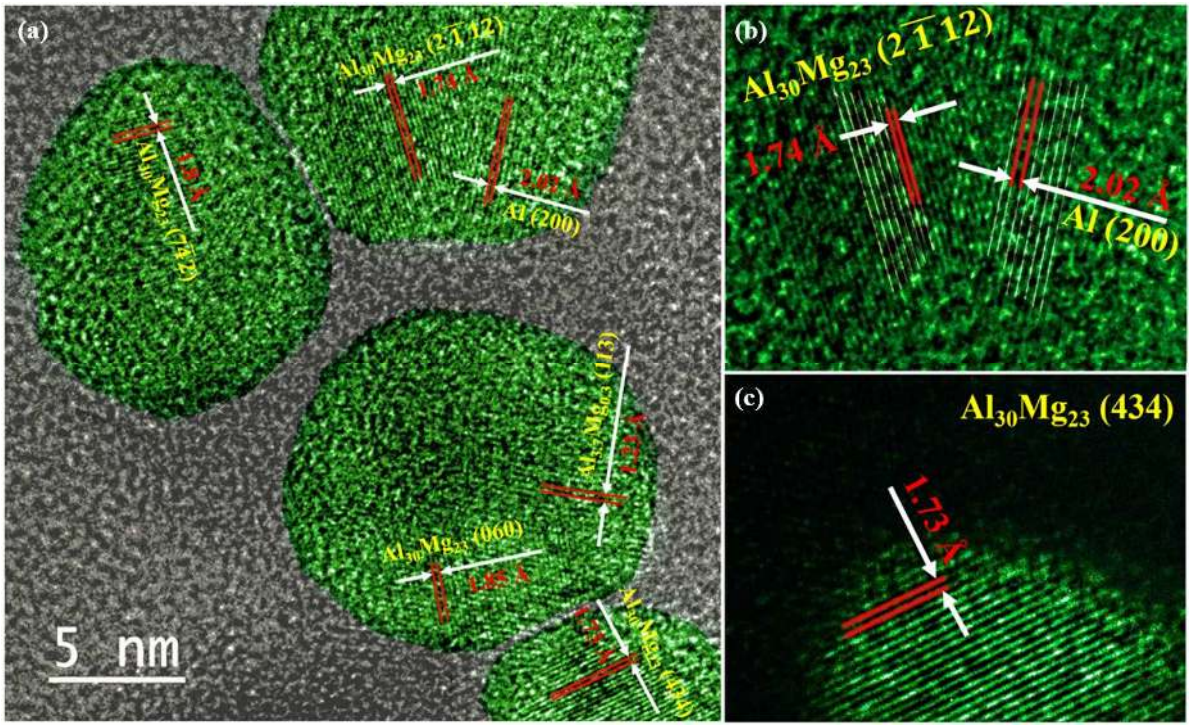


**Fig. 20.** HR-TEM showing spherical nanoparticles with various eutectic phases and the corresponding atomic planes and interplanar distances.

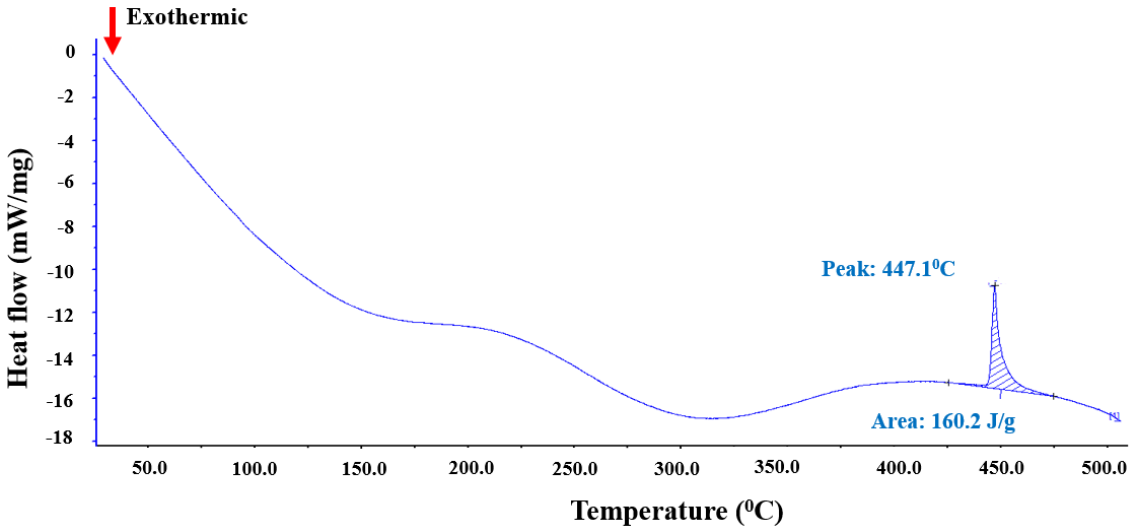


**Fig. 21.** TG-DSC of the Al-Mg eutectic alloy nanopowder synthesized by WET

## 5. Conclusion

Binary eutectic Al-Mg alloy nanoparticles are successfully synthesized by exploding the EDM cut eutectic alloy wires at a pressure of 25 kPa in the ambience of Ar and He. Various process control parameters are analysed computationally to determine the optimal conditions

to synthesize ultrafine alloy nanoparticles. The size-dependent thermodynamic and kinetic description is formulated to explain the formation mechanism, nucleation and growth rates, coalescence and coagulation of alloy nanoparticles. Also, electron microscopic studies are carried out to characterize the microstructural features of the synthesized alloy nanoparticles. The following key conclusions are made based on the present study:

- The gas-phase kinetic modelling has shown that higher the mean free path and lower the collision flux, lower is the resulting nanoparticle size which could be achieved by low-pressure electric explosions.
- The coalescence rate higher than the coagulation rate resulted in spherical nanoparticles and the adsorption controlled growth mechanism resulted in their polydispersion.
- A new $Al_{30}Mg_{23}$ phase with an Al to Mg atomic ratio of 1.304 is formed upon explosion because of the non-equilibrium quenching process and the probabilistic pair-up of the components during the gas-phase reactions and subsequent non-equilibrium phase transformations. The deviation from the equilibrium composition could also be attributed to the size-effect which alters the phase boundaries of the resulting coexisting phases.
- The SEM study confirmed the spherical morphology of the eutectic alloy nanoparticles and the EDAX mapping performed confirmed a varied concentration of Al and Mg. The HRTEM study justified that the spherical alloy nanoparticles size is lognormally distributed and the SAED ring patterns confirmed their crystalline nature and the presence of various phases.
- The STEM study through the line-EDS has shown that the Al concentration is more than that of Mg across the alloy nanoparticle which is in tandem with the phase composition predictions by the equilibrium phase diagram.
- The TG-DSC thermal signature of the Al-Mg eutectic nanopowder indicated a melting temperature of $447.1^0$C, which is a combined result of eutectic alloying and size-effect. The enthalpy of fusion is 160.2 J/g which is very low compared to that of Al and Mg and it could be inferred that this will tremendously reduce the ignition temperature and enhance the burning rate of the propellants embedded with Al-Mg eutectic nanoparticles.
- The combination of reduced melting temperature and fusion enthalpy of the Al-rich Al-Mg eutectic alloy nanopowder is expected to reduce the two-phase flow losses and the aluminium agglomeration in the rocket plume which further reduces its traceability. In the light of this, the Al-Mg eutectic nanoparticles are proposed as a viable substitute for the pure nano-Al powders in solid rocket propellants and other high energy applications.

## Acknowledgements:

This work is financially and technologically supported by Centre of Propulsion Technology (CoPT), National Centre for Combustion Research and Development (NCCRD) and High-

Voltage Laboratory, Indian Institute of Technology Madras. Comments, stimulating suggestions and help of Dr Jayaraman and research scholars Rajendra Rajak and S. Ganesan in gas kinetics study and high-speed imaging are greatly acknowledged.

## References:

[1] N.V. Mantzaris, Liquid-phase synthesis of nanoparticles: Particle size distribution dynamics and control, Chemical Engineering Science, 60 (2005) 4749-4770. https://doi.org/10.1016/j.ces.2005.04.012.

[2] K.K. Caswell, C.M. Bender, C.J. Murphy, Seedless, surfactantless wet chemical synthesis of silver nanowires, Nano Letters, 3 (2003) 667-669. https://doi.org/10.1021/nl0341178.

[3] K.A. Kusters, S.E. Pratsinis, Strategies for control of ceramic powder synthesis by gas-to-particle conversion, Powder Technology, 82 (1995) 79–91. https://doi.org/10.1016/0032-5910(94)02892-R.

[4] M. Koike, D. Li, H. Watanabe, Y. Nakagawa, K. Tomishige, Comparative study on steam reforming of model aromatic compounds of biomass tar over Ni and Ni-Fe alloy nanoparticles, Appl. Catal. A Gen. 506 (2015) 151–162. doi:10.1016/j.apcata.2015.09.007.

[5] F.E. Kruis, H. Fissan, A. Peled, Synthesis of nanoparticles in the gas phase for electronic, optical and magnetic applications-a review, J. Aerosol Sci., 29 (1998) pp. 511-535. doi:10.1158/1535-7163.MCT-08-1135.ATR.

[6] N.E. Motl, E. Ewusi-Annan, I.T. Sines, L. Jensen, R.E. Schaak, Au-Cu alloy nanoparticles with tunable compositions and plasmonic properties: Experimental determination of composition and correlation with theory, J. Phys. Chem. C. 114 (2010) 19263–19269. doi:10.1021/jp107637j.

[7] B. Palaszewski, R. Powell, Launch vehicle performance using metallized propellants, J. Propuls. Power. 10 (1994) 828–833. doi:10.2514/3.23821.

[8] B. Palaszewski, Metallized propellants for the human exploration of Mars, Sci. Technol. Ser. 89 (1997) 677–689. https://doi.org/10.2514/3.23821.

[9] A. Gany, D.W. Netzer, Fuel Performance Evaluation for the Solid-Fueled Ramjet, Int. J. Turbo Jet Engines. 2 (1985) 157–168. doi:10.1515/TJJ.1985.2.2.157.

[10] Y. Aly, M. Schoenitz, E.L. Dreizin, Ignition and combustion of mechanically alloyed Al-Mg powders with customized particle sizes, Combust. Flame. 160 (2013) 835–842. doi:10.1016/j.combustflame.2012.12.011.

[11] E. Beloni, V.K. Hoffmann, E.L. Dreizin, Combustion of decane-based slurries with metallic fuel additives, J. Propuls. Power. 24 (2008) 1403–1411. doi:10.2514/1.28042.

[12] Y.L. Shoshin, R.S. Mudryy, E.L. Dreizin, Preparation and characterization of energetic Al-Mg mechanical alloy powders, Combust. Flame. 128 (2002) 259–269. doi:10.1016/S0010-2180(01)00351-0.

[13] T.A. Roberts, R.L. Burton, H. Krier, Ignition and combustion of aluminum magnesium alloy particles in O2 at high pressures, Combust. Flame. 92 (1993) 125–143. doi:10.1016/0010-2180(93)90203-F.

[14] Y. Aly, E.L. Dreizin, Ignition and combustion of Al·Mg alloy powders prepared by different techniques, Combust. Flame. 162 (2015) 1440–1447. doi:10.1016/j.combustflame.2014.11.010.

[15] M. Schoenitz, T.S. Ward, E.L. Dreizin, Fully dense nano-composite energetic powders prepared by arrested reactive milling, Proc. Combust. Inst. 30 (2005) 2071–2078. doi:10.1016/j.proci.2004.08.134.

[16] J.H. O'Neill, U.S. Patent 1532930, 1925.

[17] J.H. De Boer, U.S. Patent 2325667 (Flash Lamp), 1943.

[18] A.. Sidorov, I.. Kravchenko, V.. Antonov, M.. Arsh, F.. Madyakin, L.. Gudoshnikova, S. Ugol'kova, Soviet Patent SU237041, 1969.

[19] H. Habu, Keikinzoku 58, 2008.

[20] M.A. Machado, D.A. Rodriguez, E.L. Dreizin, E. Shafirovich, Chemical Gas Generators Based on Mechanically Alloyed Al·Mg Powder Marco, in: Mater. Res. Soc. Symp. Proceeding, Materials Research Society, 2015: pp. 27–32. doi:10.1557/opl.2015. 287.

[21] G. Rossi, A. Rapallo, C. Mottet, A. Fortunelli, F. Baletto, R. Ferrando, Magic polyicosahedral core-shell clusters, Phys. Rev. Lett. 93 (2004) 1–4. doi:10.1103/PhysRevLett.93.105503.

[22] S. Darby, T. V. Mortimer-Jones, R.L. Johnston, C. Roberts, Theoretical study of Cu-Au nanoalloy clusters using a genetic algorithm, J. Chem. Phys. 116 (2002) 1536–1550. doi:10.1063/1.1429658.

[23] A. Aguado, L.E. González, J.M. López, Thermal properties of impurity-doped clusters: Orbital-free molecular dynamics simulations of the meltinglike transition in Li1Na 54 and Cs1Na54, J. Phys. Chem. B. 108 (2004) 11722–11731. doi:10.1021/jp049274p.

[24] C. Mottet, G. Rossi, F. Baletto, R. Ferrando, Single impurity effect on the melting of nanoclusters, Phys. Rev. Lett. 95 (2005) 1–4. doi:10.1103/PhysRevLett.95.035501.

[25] R.H. Chen, C. Suryanarayana, M. Chaos, Combustion characteristics of mechanically alloyed ultrafine-grained Al-Mg powders, Adv. Eng. Mater. 8 (2006) 563–567. doi:10.1002/adem.200600002.

[26] Y.A. Kotov, Electric explosion of wires as a method for preparation of nanopowders, J. Nanoparticle Res. 5 (2003) 539–550. doi:10.1023/B:NANO.0000006069.45073.0b.

[27] M.I. Lerner, N. V. Svarovskaya, S.G. Psakhie, O. V. Bakina, Production technology, characteristics, and some applications of electric-explosion nanopowders of metals, Nanotechnologies Russ. 4 (2009) 741–757. doi:10.1134/S1995078009110019.

[28] M.I. Lerner, A. V. Pervikov, E.A. Glazkova, N. V. Svarovskaya, A.S. Lozhkomoev, S.G. Psakhie, Structures of binary metallic nanoparticles produced by electrical

explosion of two wires from immiscible elements, Powder Technol. 288 (2016) 371–378. doi:10.1016/j.powtec.2015.11.037.

[29] T.K. Sindhu, R. Sarathi, S.R. Chakravarthy, Understanding nanoparticle formation by a wire explosion process through experimental and modelling studies, Nanotechnology. 19 (2008). doi:10.1088/0957-4484/19/02/025703.

[30] W. Kim, J.S. Park, C.Y. Suh, H. Chang, J.C. Lee, Fabrication of alloy nanopowders by the electrical explosion of electrodeposited wires, Mater. Lett. 61 (2007) 4259–4261. doi:10.1016/j.matlet.2007.01.106.

[31] W. Kim, J. shin Park, C. yul Suh, J.G. Ahn, J. chun Lee, Cu-Ni-P alloy nanoparticles prepared by electrical wire explosion, J. Alloys Compd. 465 (2008) 2007–2009. doi:10.1016/j.jallcom.2007.10.146.

[32] S. Nagasawa, T. Koishi, Y. Tokoi, T. Suzuki, T. Nakayama, H. Suematsu, K. Niihara, Determining factor of median diameter in intermetallic compound nanoparticles prepared by pulsed wire discharge, Jpn. J. Appl. Phys. 53 (2014). doi:10.7567/JJAP.53.02BD07.

[33] R. Sarathi, T.K. Sindhu, S.R. Chakravarthy, A. Sharma, K. V. Nagesh, Generation and characterization of nano-tungsten particles formed by wire explosion process, J. Alloys Compd. 475 (2009) 658–663. doi:10.1016/j.jallcom.2008.07.092.

[34] R. Sarathi, T.K. Sindhu, S.R. Chakravarthy, Generation of nano aluminium powder through wire explosion process and its characterization, Mater. Charact. 58 (2007) 148–155. doi:10.1016/j.matchar.2006.04.014.

[35] V. Sabari Giri, R. Sarathi, S.R. Chakravarthy, C. Venkataseshaiah, Studies on production and characterization of nano-Al2O 3 powder using wire explosion technique, Mater. Lett. 58 (2004) 1047–1050. doi:10.1016/j.matlet.2003.08.015.

[36] X. Gao, N. Yokota, H. Oda, S. Tanaka, K. Hokamoto, P. Chen, One step preparation of Fe–FeO–graphene nanocomposite through pulsed wire discharge, Crystals. 8 (2018) 1–10. doi:10.3390/cryst8020104.

[37] S. Tanaka, I. Bataev, H. Oda, K. Hokamoto, Synthesis of metastable cubic tungsten carbides by electrical explosion of tungsten wire in liquid paraffin, Adv. Powder Technol. 29 (2018) 2447–2455. doi:10.1016/j.apt.2018.06.025.

[38] E.M. Abdelkader, P.A. Jelliss, S.W. Buckner, Metal and Metal Carbide Nanoparticle Synthesis Using Electrical Explosion of Wires Coupled with Epoxide Polymerization Capping, Inorg. Chem. 54 (2015) 5897–5906. doi:10.1021/acs.inorgchem.5b00697.

[39] M.I. Lerner, E.A. Glazkova, A.S. Lozhkomoev, N. V. Svarovskaya, O. V. Bakina, A. V. Pervikov, S.G. Psakhie, Synthesis of Al nanoparticles and Al/AlN composite nanoparticles by electrical explosion of aluminum wires in argon and nitrogen, Powder Technol. 295 (2016) 307–314. doi:10.1016/j.powtec.2016.04.005.

[40] W. Kim, J.S. Park, C.Y. Suh, S.W. Cho, S. Lee, I.J. Shon, Synthesis of TiN nanoparticles by explosion of Ti wire in nitrogen gas, Mater. Trans. 50 (2009) 2897–2899. doi:10.2320/matertrans.M2009297.

[41] C.S. Wong, B. Bora, S.L. Yap, Y.S. Lee, H. Bhuyan, M. Favre, Effect of ambient gas

species on the formation of Cu nanoparticles in wire explosion process, Curr. Appl. Phys. 12 (2012) 1345–1348. doi:10.1016/j.cap.2012.03.024.

[42] R. Ferrando, J. Jellinek, R.L. Johnston, Nanoalloys: From theory to applications of alloy clusters and nanoparticles, Chem. Rev. 108 (2008) 845–910. doi:10.1021/cr040090g.

[43] P. Ranjan, L.S. kumar, H. Suematsu, S.R. Chakravarthy, R. Jayaganthan, R. Sarathi, Thermodynamic analysis of ZnO nanoparticle formation by wire explosion process and characterization, Ceram. Int. 43 (2017) 6709–6720. doi:10.1016/j.ceramint.2017.02.069.

[44] W. Hume-rothery, G.W. Mabbott, K.M.C. Evans, S.H. Carpenter, The freezing points, melting points, and solid solubility limits of the alloy of silver and copper with the elements of the B sub-groups, Pholosophical Trans. A 721 (1934) 1–97. https://doi.org/10.1098/rsta.1934.0014

[45] H. Brodowsky, H.-J. Schaller, Thermochemistry of Alloys Recent Developments of Experimental Methods, 1989. doi:10.1007/978-94-009-1027-0.

[46] K. Miyajima, N. Fukushima, H. Himeno, A. Yamada, F. Mafuné, Breakdown of the hume-rothery rules in sub-nanometer-sized ta-containing bimetallic small clusters, J. Phys. Chem. A. 113 (2009) 13448–13450. doi:10.1021/jp908415y.

[47] W. M. Haynes, ed., CRC Handbook of Chemistry and Physics, 96th Edition (Internet Version), CRC Press/Taylor and Francis, Boca Raton, FL, 2016.

[48] W.M. Haynes, Vapour pressure of the metallic elements, in: CRC Handb. Chem. Phys., CRC Press/Taylor and Francis, Boca Raton, FL, 2015.

[49] M. Karbalaei Akbari, R. Derakhshan, O. Mirzaee, A case study in vapor phase synthesis of Mg-Al alloy nanoparticles by plasma arc evaporation technique, Chem. Eng. J. 259 (2015) 918–926. doi:10.1016/j.cej.2014.08.053.

[50] R.E. Honing, D.A. Karamar, Vapor Pressure Data for the Solid and Liquid Elements, in: RCA Rev. 30, New York, U.S., 1969: pp. 285–305.

[51] S. Xiao, W. Hu, W. Luo, Y. Wu, X. Li, H. Deng, Size effect on alloying ability and phase stability of immiscible bimetallic nanoparticles, Eur. Phys. J. B, 54 (2006) 479–484. https://doi.org/10.1140/epjb/e2007-00018-6.

[52] M.S. Daw, M.I. Baskes, Embedded-atom method: Derivation and application to impurities, surfaces, and other defects in metals, Phys. Rev. B. 29 (1984) 6443–6453. doi:10.1103/PhysRevB.29.6443.

[53] V.P. Filippova, S.A. Kunavin, M.S. Pugachev, Calculation of the parameters of the Lennard-Jones potential for pairs of identical atoms based on the properties of solid substances, Inorg. Mater. Appl. Res. 6 (2015) 3–6. doi:10.1134/S2075113315010062.

[54] V.A. Lubarda, On the effective lattice parameter of binary alloys, Mech. Mater. 35 (2003) 53–68. doi:10.1016/S0167-6636(02)00196-5.

[55] E. Roduner, Nanoscopic materials size dependent phenomena, RSC Publishing, Cambridge, U.K., 2006. doi:10.1039/9781847557636.

[56] G.S. Sarkisov, P. V. Sasorov, K.W. Struve, D.H. McDaniel, State of the metal core in nanosecond exploding wires and related phenomena, J. Appl. Phys. 96 (2004) 1674–1686. doi:10.1063/1.1767976.

[57] R.B. Baksht, S.I. Tkachenko, V.M. Romanova, A.R. Mingaleev, V.I. Oreshkin, A.E. Ter-Oganes'yan, T.A. Khattatov, T.A. Shelkovenko, S.A. Pikuz, Stratification dynamics and the development of electrothermal instability at the wire explosion, Tech. Phys. 58 (2013) 1129–1137. doi:10.1134/S1063784213080021.

[58] A. V. Pervikov, M.I. Lerner, E.A. Glazkova, V. V. Domashenko, Phase state of matter during metal and binary alloy conductor dispersion by a pulse of current, AIP Conf. Proc. 1623 (2014) 483–486. doi:10.1063/1.4898987.

[59] W.H. Qi, B.Y. Huang, M.P. Wang, Size and shape-dependent formation enthalpy of binary alloy nanoparticles, Phys. B Condens. Matter. 404 (2009) 1761–1765. doi:10.1016/j.physb.2009.02.014.

[60] K. Jayaraman, K. V. Anand, D.S. Bhatt, S.R. Chakravarthy, R. Sarathi, Production, characterization, and combustion of nanoaluminum in composite solid propellants, J. Propuls. Power. 25 (2009) 471–481. doi:10.2514/1.36490.

[61] H. Okamoto, Al-Mg (Aluminium-Mahnesium), J. Phase Equilibria. 14 (1998) 598.

[62] L.H. Liang, D. Liu, Q. Jiang, Size-dependent continuous binary solution phase diagram, Nanotechnology. 14 (2003) 438–442. doi:10.1088/0957-4484/14/4/306.

[63] N.T.K. Thanh, N. Maclean, S. Mahiddine, Mechanisms of nucleation and growth of nanoparticles in solution, Chem. Rev. 114 (2014) 7610–7630. doi:10.1021/cr400544s.

[64] F.M. Takrori, A. Ayyad, Surface energy of metal alloy nanoparticles, Appl. Surf. Sci. 401 (2017) 65–68. doi:10.1016/j.apsusc.2016.12.208.

[65] T. Wen, L.N. Brush, K.M. Krishnan, A generalized diffusion model for growth of nanoparticles synthesized by colloidal methods, J. Colloid Interface Sci. 419 (2014) 79–85. doi:10.1016/j.jcis.2013.12.018.

[66] T. Hawa, M.R. Zachariah, Coalescence kinetics of unequal sized nanoparticles, J. Aerosol Sci. 37 (2006) 1–15. doi:10.1016/j.jaerosci.2005.02.007.

[67] J. Tu, TEM Nano-Moiré Pattern Analysis of a Copper/Single Walled Carbon Nanotube Nanocomposite Synthesized by Laser Surface Implanting, C. 4 (2018) 19. doi:10.3390/c4010019.

[68] J.K. Sambamurthi, E.W. Price, R.K. Sigman, Aluminum agglomeration in solid-propellant combustion, Am. Inst. Aeronaut. Astronaut. Aerosp. Sci. Meet. 22 (1983) 1132–1138. https://doi.org/10.2514/3.48552.

# Graphical Abstract

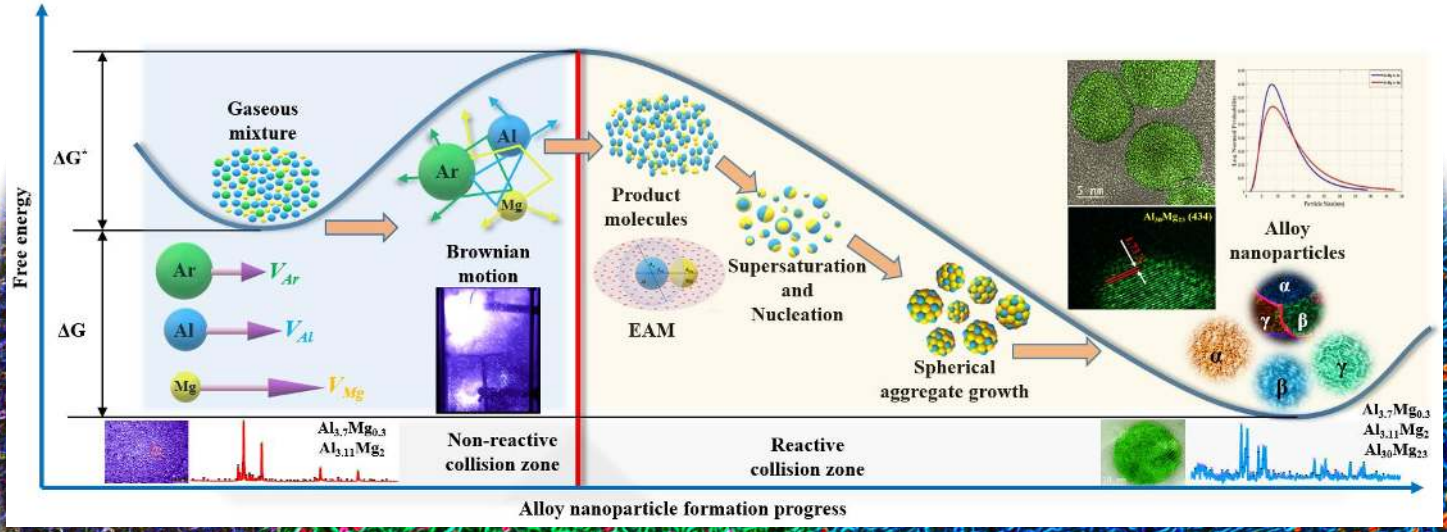


**Synthesis of Multiphase Binary Eutectic Al-Mg Alloy-Nanoparticles by Electrical Wire Explosion Technique for High-Energy Applications, its Characterisation and Size-Dependent Thermodynamic and Kinetic Study**